Propeller Blade Design inside Boundary Layer

Inverse Design of Boundary-Layer-Ingesting Propulsors

Archisman Acharya

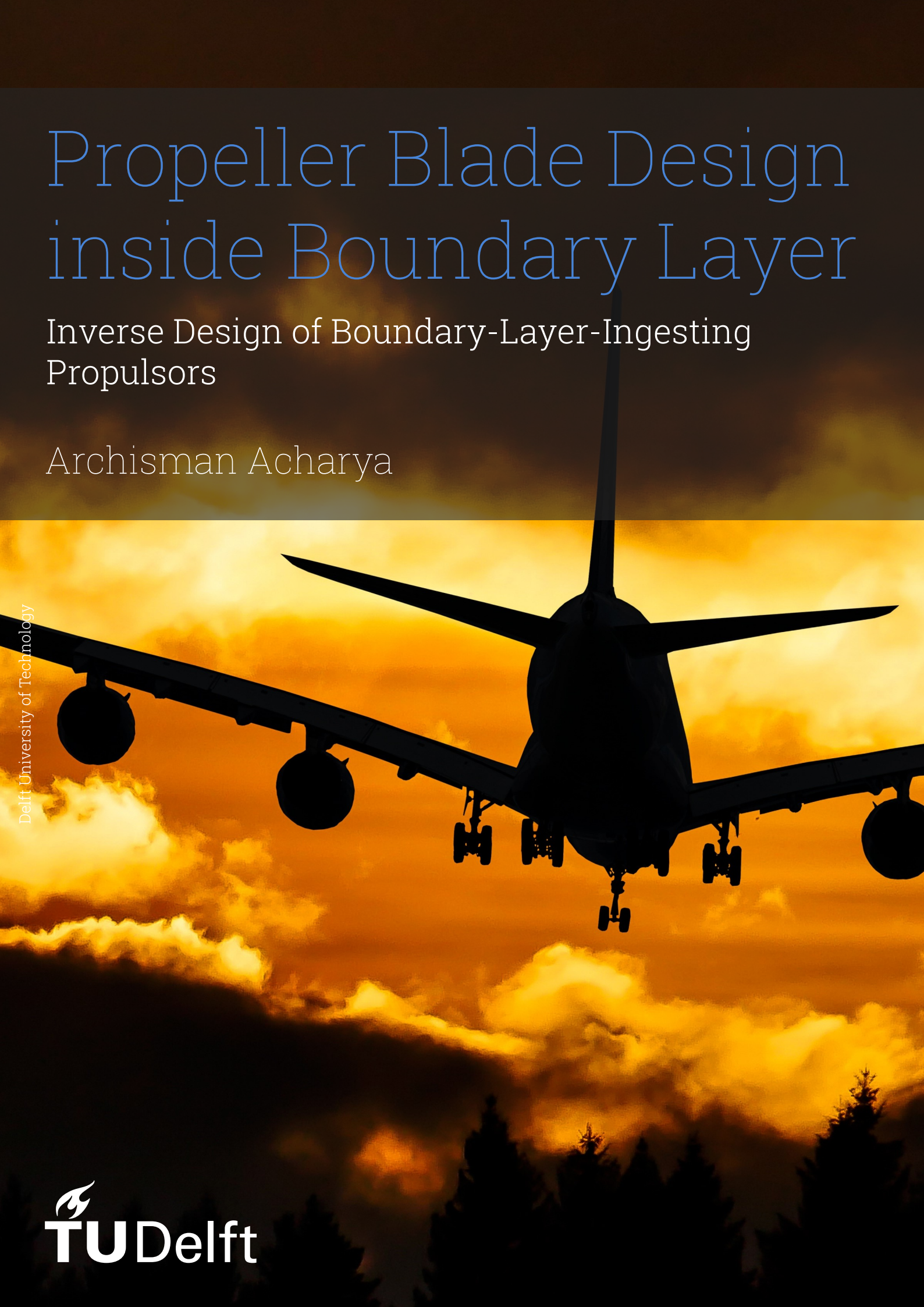

Delft University of Technology

TU Delft

Propeller Blade Design inside Boundary Layer

Inverse Design of Boundary-Layer-Ingesting Propulsors

by

Archisman Acharya

to obtain the degree of Master of Science

at the Delft University of Technology,

to be defended publicly on Wednesday January 14, 2024 at 1:00 PM.

Thesis Supervisor:	Dr. G. Eitelberg
Thesis Mentor:	Dr. A. Heidebrecht
Thesis Committee Chair:	Dr. T. Sinnige
External Examiner:	Dr. R. Merino Martinez
Faculty:	Faculty of Aerospace Engineering, Delft
Student Number	5298563
Thesis Duration:	May 2025 - January 2026

Cover:	Aircraft Flying in the Sunset by Gerhard Gellinger
Style:	TU Delft Report Style, with modifications by Daan Zwaneveld and Archisman Acharya

An electronic version of this thesis is available at `http://repository.tudelft.nl/`.

TU Delft

Preface

This thesis is submitted in partial fulfilment of the requirements for the degree of Master of Science in Aerospace Engineering at Delft University of Technology and marks the end of my academic journey for now. The work was carried out within the Faculty of Aerospace Engineering and focuses on the aerodynamic modelling, loss analysis and inverse design of propellers operating under boundary-layer-ingesting conditions.

I would like to thank my supervisor and mentor, G. Eitelberg and A. Heidebrecht, for their continuous support, guidance, and encouragement throughout this project. I would be lying if I said this was a smooth ride. At the start, I felt quite overwhelmed by the amount of new theory and concepts I was confronted with, and it was not always clear how everything fit together. Through many discussions, thoughtful feedback sessions, and a great deal of patience on their part, the bigger picture slowly started to make sense. I am genuinely grateful for the time and care they invested in helping me grow as a researcher, and for the trust they gave me as this thesis took shape. I would also like to thank Tomáš Kukučka, as this work builds directly on the foundation laid by his earlier research. With this, my time in Delft also comes to an end, bringing to a close an incredible five and a half years that have shaped me both academically and personally. I arrived in the Netherlands back in 2020, in the middle of the COVID-19 pandemic, not knowing anyone and with my family all the way across the world in Singapore. Online lectures and long days at home were the norm, and in those early months I was lucky to have my uncle and aunt, Arunabha and Anindita, whose support and reassurance helped me feel less alone and far more supported. Looking back now, the contrast with my life today could not have been greater, and it is entirely thanks to the incredible people I have met who I have the privilege to call friends now. Having moved around frequently, it has never been easy for me to call one place home, but Delft comes as close as it possibly could.

Alex and Max, thank you for getting me out of my shell and for always being open to hearing me rant about just about anything. Antra, thank you for being there for me every single time, whether things were going up or down. Job and Boris, thank you for giving me a haircut with a pasta spatula, something I will never forget. Nachiket, you have been there from the very beginning, and that has meant more than I can put into words. Emma, the best thesis buddy I could have asked for. Any day of the week, extreme weather or not, I knew you would show up to the fellowship, and I could honestly dedicate part of this thesis to you. And to all the friends I could not name individually, a huge thank you for everything.

Finally, to my family, Ma and Baba, a simple thank you will never be enough to express what I owe to you both. The sacrifices you made to give me the opportunity to study at this university and to leave home at such a young age have shaped everything that followed, and I will always be grateful for your unwavering support and trust. Brinda, I do not see myself stopping to annoy you anytime soon. I suppose that is my responsibility as an older brother, but trust me, it really helps me keep myself sane:). And Coco - I know you do not understand much more than a dog probably should, but trust me, you have helped more than you will ever know.

Archisman Acharya
Delft, January 2026

Contents

List of Figures

List of Tables

Nomenclature

Abbreviations

Abbreviation	Definition
AD	Actuator Disk
BLI	Boundary Layer Ingestion
BL	Boundary Layer
BOR	Body of Revolution
CFD	Computational Fluid Dynamics
CP	Control Point
ESDU	Engineering Sciences Data Unit
ISA	International Standard Atmosphere
PBM	Propeller Blade Model
TE	Trailing Edge

Symbols

Symbol	Definition	Unit
A	Area	[m^2]
c	Blade chord	[m]
H	Boundary layer shape factor	[-]
L_{mix}	Mixing loss per unit span	[W/m]
p	Static pressure	[Pa]
Δp	Pressure jump across actuator disk	[Pa]
P	Power	[W]
$\dot{P}$	Power flux	[W]
r	Radial coordinate	[m]
R	Actuator disk radius	[m]
T	Thrust	[N]
U	Velocity magnitude	[m/s]
U_e	Boundary layer edge velocity	[m/s]
V	Velocity	[m/s]
x	Axial coordinate	[m]
δ	Boundary layer thickness	[m]
δ_1	Displacement thickness	[m]
δ_2	Momentum thickness	[m]
ν	Kinematic viscosity	[m^2/s]
ρ	Air density	[kg/m^3]
ϕ	Local surface angle	[rad]

Symbol	Definition	Unit
Γ	Vortex strength	[m^2/s]

1

Introduction

Commercial aviation faces increasing pressure to reduce fuel burn and emissions while maintaining range, payload capability, and economic viability. While conventional tube-and-wing aircraft with underwing podded engines have achieved steady improvements through higher bypass ratios, aerodynamic refinement, and lighter structures, further gains are expected to require more integrated propulsion concepts. One such concept is boundary layer ingestion (BLI), in which a propulsor is placed in the low-momentum wake of a body to partially recover the velocity deficit and reduce the shaft power required for a given mission.

When a propeller or fan operates in BLI conditions, it ingests a strongly non-uniform inflow shaped by the body boundary layer and the overall aircraft layout. This complicates both aerodynamic analysis and blade design. Classical propeller design methods typically assume uniform or weakly sheared inflow and prescribed radial loading, and are therefore not directly applicable to BLI. High-fidelity computational fluid dynamics can in principle resolve these flows, but remains too costly and opaque for systematic exploration of radial loading strategies and their effect on the wake.

This thesis develops a low-fidelity but physically informed actuator-disk-based framework to study boundary layer ingestion for a body of revolution. The model combines three elements: a potential flow solution for the outer inviscid flow and actuator-disk-induced velocities, a boundary layer model providing the non-uniform inflow and displacement effect, and a slipstream correction model that redistributes mass and momentum downstream to ensure consistency with the ingested boundary layer and global conservation laws. Together, these elements yield a coupled flow description that captures the key physics of BLI while remaining computationally efficient and transparent.

Within this framework, the actuator disk is not restricted to a single uniformly loaded surface. Instead, multiple disks with different radii can be combined to approximate prescribed radial pressure jump distributions, such as an approximately elliptical loading or loadings biased towards the inner part of the slipstream. These configurations are evaluated using wake-based metrics. An axisymmetric mixing-loss metric quantifies the tendency of the slipstream to mix and dissipate energy downstream, while power-flux measures compare the kinetic power in the inlet boundary layer, the downstream wake, and an equivalent clean free stream.

To connect actuator-disk-level loading trends to practical propeller designs, the thesis formulates an

inverse blade design method. Prescribed radial pressure jump distributions and local inflow conditions are translated into three-dimensional blade geometries using airfoil polar data and simplified blade element relations. This provides a direct link between abstract loading concepts and blade shapes that could in principle be manufactured.

The scope of the work is deliberately restricted to maintain tractability and focus on the dominant physical mechanisms. The body is modelled as an axisymmetric body of revolution, the outer flow is assumed incompressible and inviscid, and the boundary layer is steady and axisymmetric. Structural, acoustic, and aeroelastic constraints are not considered. Within these assumptions, the aim is not to optimise a specific propeller, but to understand how radial pressure jump distributions influence wake mixing and power flux in boundary layer ingestion, and to assess whether favourable distributions can be realised as plausible blade geometries.

The remainder of this thesis is organised as follows. chapter 2 reviews the relevant literature on boundary layer ingestion, actuator disk theory, and propeller operation in non-uniform inflow. chapter 3 defines the research problem, identifies the knowledge gap, and outlines the preliminary methodology. chapter 4 presents the coupled actuator-disk-based flow model, including the potential flow formulation, boundary layer modelling, slipstream correction, and the extension from a single to multiple actuator disks. In chapter 5, mixing loss and power-flux metrics are introduced and applied to assess the effect of different loading distributions. chapter 6 describes the inverse blade design method used to translate actuator-disk loading into three-dimensional blade geometries, followed by the resulting blade designs in chapter 7. chapter 8 provides a validation of the proposed approach through comparison with an existing boundary-layer-ingesting propeller design. Finally, chapter 9 summarises the main conclusions and provides recommendations for future work.

2

Literature Study

Before the start of the thesis, a literature study was conducted in the field of BLI. The main goal of this literature study is to gain some insights and a general overview of the topic, get up to date with the past and present research, and determine the current technology readiness level of this technology. This would act as the baseline of the research question that is going to be worked on during this master's thesis at Delft University of Technology.

2.1. Boundary Layer Ingestion

Boundary Layer Ingestion is an aeropropulsive integration concept that seeks to enhance the aircraft efficiency by taking advantage of the interaction between the airframe and the propulsion system. Unlike traditional aircraft designs, where engines are mounted to minimise aerodynamic interference, BLI places the propulsion system in such a manner that allows to ingest and re-energise the aircraft boundary layer. This concept has gained attention in recent years as a means of improving fuel efficiency. Some of the first investigations into the application BLI for air propulsion were carried out by McLemore[18]

As explained by Arntz [4]: The thrust force produced by a propulsor is directly proportional to the difference of the velocities, whereas the power consumed by the propulsor is directly proportional to the square of the velocities. This implies that for a given thrust, the power required goes up with increasing inlet velocity, and hence, placing the propulsor in the wake of the airframe might be beneficial. As derived by Plas [19]: we consider the force, F, produced by an engine as follows:

$$F = \dot{m}(V_2 - V_1) = \dot{m}\Delta V \tag{2.1}$$

where V_1 and V_2 are respectively the inlet and outlet axial velocity and $\dot{m}$ is the massflow through the engine. Similarly, the mechanical power, P, supplied by the propulsion system is:

$$P = \frac{\dot{m}}{2}(V_2^2 - V_1^2) = F(V_1 + \frac{\Delta V}{2}) \tag{2.2}$$

2.1.1. Momentum, power and Exergy Balance

The various techniques used for quantifying the performance of BLI aircraft can be categorized by momentum integral methods, energy integral methods and exergy integral methods.

Momentum integral approaches establish a momentum equilibrium to determine drag and thrust. However, applying these methods to Boundary Layer Ingestion (BLI) configurations can be challenging, as certain streamtubes are influenced by both the propulsor and the airframe, carrying only information about the net force. Consequently, these methods often rely on significant assumptions and may overlook interaction effects between the airframe and the propulsor. Despite being less reliable than power- and exergy-based methods for configurations with strong propulsor–airframe interaction, momentum-integral approaches remain widely used in early design because they require only limited flow information (or simplified assumptions) and can be evaluated at low computational cost [17, 20, 12].

The first energy integral method, introduced by Drela [8], marked a major advancement in performance assessment for BLI configurations. The Power Balance Method (PBM) enables the evaluation of an aircraft's propulsive power by establishing a power balance over the control volume S, as illustrated in Figure 2.1

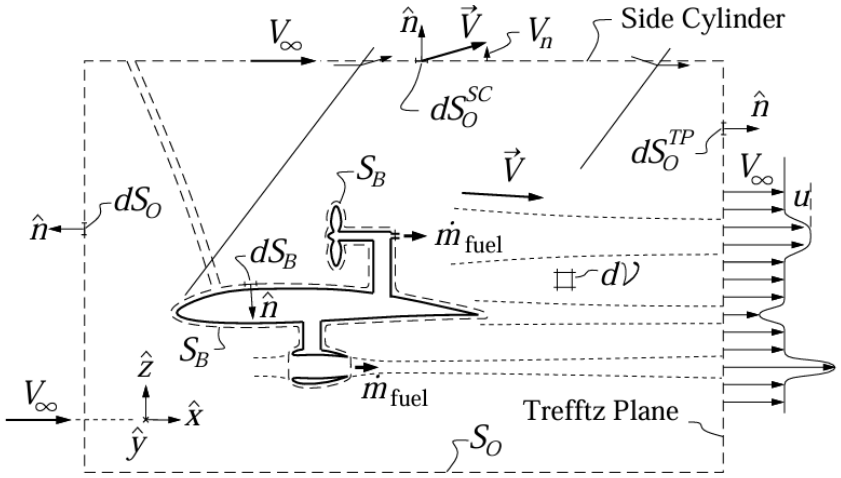

Figure 2.1: Control Volume around an arbitrary propeller aerodynamic body used by the PBM [8]

The sink and the source terms are equated and are shown in Equation 2.3:

$$P_S + P_V + P_K = \dot{\epsilon} + \phi \tag{2.3}$$

The term P_S represents the net propulsor shaft power, calculated by integrating the force multiplied by velocity overall moving surfaces. This term accounts for power contributions such as that provided by a propeller. The term P_V refers to the volumetric power generated by fluid expansion against atmospheric pressure, which becomes significant when heat is added to the system, as in the case of a turbojet engine. Lastly, the term P_K represents the net inflow rate of mechanical energy into the propulsor. This term is relevant when the propulsor is located outside the control volume, such as the one positioned beneath the body in Figure 2.1. The right side of the equation represents the outflow of power from the control volume. $\dot{\epsilon}$ represents the net mechanical energy outflow through the Trefftz plane and the side boundaries. The term ϕ is the dissipation of kinetic energy into heat within the control volume.

While momentum-based and power-based control-volume analyses provide a clear framework to quantify the theoretical benefit of ingesting low-momentum flow, they also highlight that the net benefit is strongly dependent on how losses are generated and redistributed in the propulsor–airframe system. In particular, the power-balance formulation provides a direct link between the imposed momentum addition, the wake non-uniformity, and the irreversible losses that occur during wake mixing and recovery. This perspective is commonly used to interpret BLI performance beyond ideal actuator-disk arguments, and to explain why the expected propulsive benefit can be reduced by additional dissipation in the propulsor, ducting, and wake [9, 20, 12].

The PBM enables a clear calculation of the BLI benefit using a flow field around an aircraft, obtained either through Computational Fluid Dynamics (CFD) simulations or detailed wind tunnel measurements. However, the main drawback of this method is its reliance on a detailed flow field, making it less suitable for conceptual design or design optimisation processes. The third category of methods for evaluating BLI configuration performance is the exergy balance methods, first introduced by Arntz [4]. These methods combine a momentum balance with the first and second laws of thermodynamics. Exergy, the conserved quantity in this approach, represents the portion of energy that can theoretically be converted into useful work. A key advantage of this method over the PBM is its ability to account for thermal energy in addition to mechanical power. However, like the PBM, it also requires a resolved flow field as input.

2.1.2. Propellers in Boundary Layers

The propulsive efficiency is often represented as:

$$\eta_p = \frac{TV_\infty}{P_{\text{shaft}}}, \tag{2.4}$$

where TV_∞ is the *useful propulsive power* delivered to the aircraft and P_{shaft} is the mechanical power supplied at the shaft. The difference between these quantities represents losses, which can be associated with (i) kinetic-energy flux left in the slipstream (i.e. the wake kinetic-energy excess) and (ii) aerodynamic losses on the blades such as profile drag and, for a real propeller, losses related to swirl and viscous dissipation [7, 16].

In an idealised actuator-disk interpretation (neglecting swirl and profile losses), the shaft power is primarily used to increase the axial momentum of the flow, and the loss can be interpreted as the kinetic-energy increase carried away by the wake. This makes the propulsive efficiency strongly linked to the magnitude of the induced velocity relative to the flight speed: for a given thrust level, operating at low V_∞ typically requires a higher induced velocity, increasing the wake kinetic-energy excess and reducing η_p [10].

A common non-dimensional parameter used to describe propeller operating condition is the advance ratio:

$$J = \frac{V_\infty}{nD}, \tag{2.5}$$

where n is the rotational speed (rev/s) and D is the propeller diameter. For a given propeller geometry, η_p is *not* a monotonic function of J over the full operating range: efficiency typically rises from low values at very small J, reaches a maximum near a design condition, and then decreases again as J becomes large and the blades operate at low loading [10, 7]. The exact $\eta_p(J)$ behaviour depends on blade geometry, Reynolds number, and operating constraints (e.g. fixed pitch and fixed RPM versus variable pitch), but the advance ratio remains a convenient parameter to compare operating points.

2.1.3. Power Saving Coefficient

Smith[25] employed an Actuator Disk model to analyse power savings and efficiency, linking these metrics to wake characteristics such as the shape factor, displacement thickness, and wake recovery. This approach accounts for the non-uniformity of the wake. A Power Saving Coefficient (PSC) was introduced to quantify the benefits of wake ingestion. Smith [25] theoretically concluded that maximum efficiency is achieved when the wake is fully recovered, meaning the velocity deficit behind the propulsor is eliminated. However, the analysis did not address the role of pressure in the solution, particularly how the increased pressure behind the propeller adjusts to ambient conditions, which in turn affects the axial velocity. Smith's [25] examples demonstrated a potential power reduction of up to 20% for complete wake recovery, based on the velocity relative to the freestream flow. The study emphasised the importance of incorporating interaction effects into the design process for practical applications.

2.1.4. Propulsors in distorted and non-uniform inflow

A defining characteristic of boundary layer ingestion is that the propulsor operates in a non-uniform inflow field, both in the radial direction (due to the boundary-layer velocity deficit) and, for realistic airframes, potentially also circumferentially. In such conditions, the propulsor loading is no longer determined by a single free-stream velocity, and the resulting slipstream can exhibit strong shear layers that influence downstream mixing and losses. This means that propulsor performance predictions and design methods developed for uniform inflow are not directly applicable to BLI configurations.

A range of engineering-level approaches have therefore been developed to predict propeller loading and performance in prescribed non-uniform inflow conditions. In particular, actuator-disk and blade-element/momentum-type methods can be adapted to accept a spatially distributed inflow profile and estimate the corresponding blade loading and forces at low computational cost. An example is the work of van Arnhem, who developed an engineering approach to estimate blade loading in nonuniform flow and applied it to installed pusher propeller configurations with boundary-layer-type inflow profiles [2, 3].

However, most distributed-inflow propulsor methods treat the inflow distortion as a prescribed input and do not explicitly model the coupled interaction with the airframe boundary layer, including displacement effects and the mutual influence between the propulsor-induced pressure field and the upstream viscous flow. For BLI, this coupling is central: the propulsor both ingests and modifies the boundary layer, and the resulting wake structure and mixing losses depend on the combined propulsor–airframe solution. This motivates the coupled framework adopted in the present thesis, where the loading distribution can be varied while accounting for the interaction with a body boundary layer and the resulting slipstream development.

2.1.5. Examples of propulsion system integrated in the boundary layer

D8 Configuration

One of the earliest and most notable advancements in the field of BLI was the D8 configuration, initially conceptualised in 2010 by Greitzer [11] as part of NASA's N+3 program. Illustrated in Figure 2.2, the D8 design features a distinctive "double-bubble" fuselage, a twin pi-tail, and is intended to serve as an airliner for the 180-passenger, 3000-nautical-mile range market, with a target Entry Into Service (EIS) year of 2035. The engines are positioned near the rear stagnation point of the fuselage, integrated flush with the top surface, and ingest approximately 40% of the fuselage boundary layer. The fuselage also functions as a diffuser and flow aligner, allowing for smaller nacelles, which reduces both drag and weight [27].

Figure 2.2: Render of the D8 Configuration[11]

A design optimization study aimed at minimizing fuel burn for the D8 configuration was conducted by Drela[8], followed by wind tunnel experiments on a 1:11 scale powered model, as presented by Uranga[26]. The experimental results demonstrated a BLI benefit of approximately 6% when comparing the boundary layer-ingesting configuration to a conventional pylon-mounted engine setup. Uranga[26] further validated these results using the Power Balance Method (PBM), quantifying the BLI benefit at 8.6 ± 1.8%. Additionally, mission-level studies of the D8 concept reported fuel-burn reductions on the order of $\sim$36% relative to a conventional tube-and-wing baseline. It is important to note that this figure reflects the combined impact of multiple technologies and design changes (e.g. airframe aerodynamics, propulsion system integration, and operational assumptions), and cannot be attributed to BLI alone. In contrast, the isolated propulsive benefit of BLI or propulsive-fuselage integration is typically reported as a single-digit percentage change in required propulsive power under comparable operating conditions [28, 12]. For this reason, the present thesis focuses on the local aeropropulsive mechanisms (wake non-uniformity, mixing losses, and power balance) that determine the BLI contribution, rather than on total mission fuel-burn accounting.

STARC-ABL Concept

In a 2016 study, Welstead [29] introduced the Single-Aisle Turboelectric Aircraft with an Aft Boundary-Layer Propulsor (STARC-ABL), depicted in Figure 2.3. This configuration features two under-wing engines, with power transmitted electrically to a boundary-layer ingestion (BLI) fan mounted at the rear of the fuselage. Developed by NASA, the concept serves as an initial exploration into turbo-electric propulsion, aiming to determine whether the BLI benefits can offset the losses associated with power conversion. The aircraft was sized based on the mission profile of a Boeing 737 or Airbus A320, and the design was projected for an entry into service (EIS) in 2035.

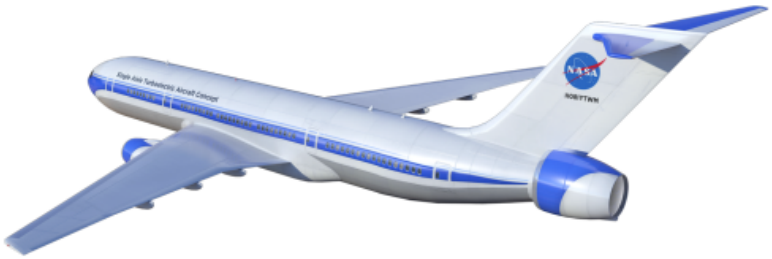

Figure 2.3: STARC-ABL concept by NASA[29]

For design optimizations, performance was estimated using a simplified approach, which involved predicting boundary layer properties by interpolating existing CFD results for flow over the fuselage. Notably, the propulsion system weight of the turbo-electric configuration was found to be lighter than that of the reference system. This weight reduction was attributed to the smaller diameter of the turbofan engines and the higher efficiency of the fuselage-mounted fan. The turbo-electric concept showed improvements of 15% in thrust-specific fuel consumption and 12% in mission fuel burn when compared to a reference configuration without the fuselage fan.

The NOVA configuration

As part of work conducted at the French National Aerospace Research Centre (ONERA) in 2016, Wiart [30] introduced four Nextgen ONERA Versatile Aircraft (NOVA) configurations. Designed for entry into service (EIS) in 2025, these aircraft were sized to carry 180 passengers over a range of approximately 5,600 km. One of the configurations featured BLI semi-buried turbofan engines located at the aft fuselage, designed to ingest about 40% of the fuselage b‘oundary layer. The PSC was evaluated using Reynolds-Averaged Navier-Stokes (RANS) simulations, with the fan represented as an actuator disk. Under cruise conditions, the PSC was estimated to be 5

Figure 2.4: NOVA Configuration[30]

2.2. Actuator Disk Model

The actuator disk model is a technique for analyzing rotor performance. Here, the rotor is represented as a permeable disk that allows the flow to pass through the rotor. At the same time, it is subject to the influence of surface forces. This model was originally formulated by Rankine and Froude [22]. The

classical actuator disk is based on the conservation of mass, momentum and energy This combined with the blade element analysis results in the BEM model. In Figure 2.5, a simple actuator disk model can be seen. Here, the propeller is represented as an actuator disk and as can be seen, this just simply causes a sudden jump in total pressure.

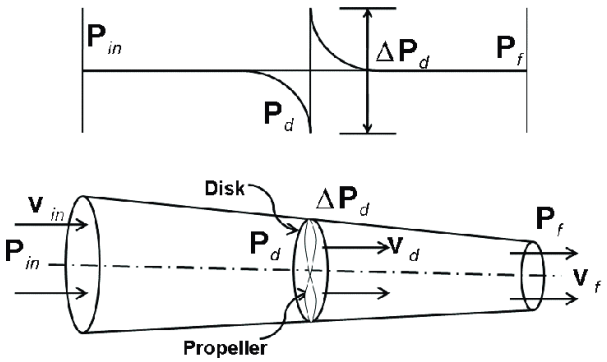

Figure 2.5: Actuator Disk Model[1]

The key assumptions of the actuator disk model are as follows:

- The actuator disk is infinitesimally thin (zero thickness).
- The outer flow is treated as steady, incompressible and inviscid (viscous effects are not resolved by the disk model).
- The formulation is axisymmetric and the loading is prescribed as a radially symmetric pressure jump (or equivalently an axisymmetric force distribution).
- In the simplest momentum-theory form, the flow in the streamtube is assumed uniform at each axial station (one-dimensional approximation).

To construct a computationally inexpensive, low-fidelity model, the propulsor can be represented as an actuator disk. The basis of this model is derived from the potential flow theory presented by van Kuik[13]. This particular model is applicable to both energy-adding and energy-extracting actuator disks. Van Kuik's [14] actuator disk model uses a series of discrete vortex rings distributed along the slipstream of the propulsor, extending downstream from the actuator disk to a prescribed location. Beyond this point, the slipstream is assumed to be fully contracted and is represented by a semi-finite vortex tube of constant radius R. Furthermore, the model imposes two boundary conditions on the slipstream:

- The velocity component normal to the slipstream must be zero.
- The slipstream surface must be force-free.

The primary input variables are the prescribed thrust and the radius of the fully contracted slipstream. The velocity induced by the vortex rings is computed using the Biot-Savart law.

2.2.1. Problems of using Actuator Disk Model

The classical actuator-disk model is a useful first-order representation of a propulsor because it replaces the detailed blade aerodynamics by a thin surface that imparts a prescribed pressure jump to the flow. In its simplest (one-dimensional) momentum-theory form, the disk is treated as having zero thickness and the pressure is discontinuous across the disk, while the flow properties upstream and downstream are assumed uniform within the streamtube [10, 16]. In this idealisation the acceleration of the flow is driven by the imposed pressure rise and is represented by a change in the streamtube velocity between

the far upstream and far wake states. In reality, the propulsor has finite thickness and a finite number of blades, so the pressure and velocity fields adjust continuously and the wake develops over a finite distance through the roll-up and diffusion of vorticity.

A second limitation is that the basic actuator-disk model does not resolve the three-dimensional vortex system generated by a real propeller (tip vortices and a trailing vortex sheet), nor the associated swirl and detailed wake structure. As a result, important loss mechanisms: such as induced power associated with the vortex wake and mixing losses due to non-uniform slipstream profiles, must be introduced through additional modelling assumptions rather than emerging directly from the solution [23, 13, 9]. More refined representations, such as lifting-line and vortex methods, model the propulsor loading as a spanwise circulation distribution that sheds vorticity into the wake, enabling a more explicit link between loading, induced velocities, and wake evolution [21, 16].

3

Problem Definition and Preliminary Methodology

The focus of this chapter is to introduce the problem that is addressed in this thesis and to explain how the planned methodology follows from it. First, the knowledge gap is identified in Section 3.1. Then, the main research question and the associated objectives are formulated in Section 3.2. Finally, the preliminary methodology that was set at the start of the project is outlined in Section 3.3, including the structure of the planned modelling and analysis steps.

3.1. Knowledge Gap

Boundary layer ingestion is a promising concept to improve the propulsive efficiency of transport aircraft by recovering part of the kinetic energy that is normally lost in the slipstream of the airframe. A propulsor that ingests the low momentum boundary layer sees a strongly non uniform inflow, which changes both the performance of the propulsor and the structure of the downstream slipstream. The potential benefit of boundary layer ingestion therefore depends critically on how the propulsor loads the ingested flow and on how much additional mixing is generated in the slipstream.

Most low-order studies of boundary layer ingestion systems make use of one dimensional actuator disk models with a uniform pressure jump across the disk or with a simple radial dependence of thrust. These models are valuable to understand global trends and to define quantities such as power saving coefficient. However, they do not systematically explore how the radial pressure jump distribution influences the structure of the slipstream, the amount of irreversible mixing, and the subsequent opportunities and constraints for real propeller blades that must operate in this environment.

In particular, there is a limited understanding of how different radial loading strategies for a propulsor in the slipstream of a body of revolution affect:

- The distribution of axial velocity in the slipstream,
- The associated mixing losses and power flux in the slipstream, and
- The resulting requirements for the radial variation of thrust that must be realised by a propeller blade.

Existing work either assumes a simple loading distribution and studies its consequences, or uses high fidelity simulations that make it difficult to scan many candidate loadings or to build physical insight into the connection between disk level loading and blade level design.

A related gap exists between low order actuator disk studies and actual blade geometries. Even when a radial pressure jump distribution has been identified as favourable at disk level, it is not obvious how this distribution translates into chord and twist distributions for a real propeller that sees a non uniform inflow. Very few studies explicitly link a prescribed boundary layer ingestion loading with an inverse blade design procedure.

The knowledge gap that this thesis addresses can therefore be summarised as follows. There is no clear and systematic framework that connects radial pressure jump distributions for a boundary layer ingesting actuator disk on a body of revolution to the resulting slipstream mixing losses and to the blade geometries that could realise such loadings.

3.2. Research Question and Objectives

The central research question of this thesis is formulated as

"How can the radial pressure jump distribution of a propulsor operating in boundary layer ingestion on a body of revolution be chosen in order to reduce losses in the slipstream, taking into account the effect of the propulsor in the upstream flow?"

This question is intentionally broad. It connects three levels of the problem: the actuator disk level, where the radial pressure jump distribution is prescribed; the slipstream level, where mixing losses and power flux are evaluated; and the blade level, where a realistic geometry must deliver the required radial loading under non uniform inflow.

To make this question tractable, the thesis is structured around the following sub questions:

- How does the choice of radial pressure jump distribution affect slipstream velocity profiles, power flux and mixing losses for a given thrust?
- How can losses in the slipstream of a boundary layer ingestion propulsor be quantified in terms of power flux and mixing?
- How can an improved radial pressure jump distribution be translated into a practical blade design with chord and twist distributions?

With this research question and the subsequent sub questions, the thesis can be broken down and divided into the following smaller objectives:

- Develop a low order axisymmetric flow model that combines a body of revolution, a representation of the boundary layer and slipstream, and one or more actuator disks that can impose arbitrary radial pressure jump distributions.
- Define and implement measures for mixing loss and power flux in the slipstream of the body and actuator disk system, in order to quantify how different radial loadings affect the quality of the ingested and expelled flow.
- Explore families of radial pressure jump distributions, with particular attention to shapes that resemble elliptical loading and to the split of thrust between the region inside the body boundary layer and the outer region.
- Formulate an inverse blade design method that, for a given design condition and for a given radial pressure jump distribution, produces spanwise chord and twist distributions and a three

dimensional propeller geometry that can deliver that loading under a simplified representation of the inflow.

- Use the combination of the flow model, the mixing loss analysis and the inverse blade design results to identify qualitative design guidelines for radial loading in boundary layer ingestion propulsors on bodies of revolution.

The preliminary methodology that was defined at the start of the project describes how these objectives are to be addressed.

3.3. Preliminary Methodology

The preliminary methodology specifies how the problem was intended to be approached at the start of the thesis. It connects the research question and objectives to a set of modelling, analysis and design steps. The logic of this plan is illustrated in the methodology overview diagram in Figure 3.1. The figure shows a sequence of blocks that starts from the problem definition and then progresses through flow model development, radial loading exploration, mixing loss and power flux analysis, inverse blade design and, finally, validation and design guidelines.

The following subsections explain this plan in more detail. They describe the intended objective and problem formulation, the design variables and constraints that were considered, the planned structure of the modelling loop, and the expected outputs of the methodology.

3.3.1. Objective and Problem Formulation

The overall objective of the planned methodology is to identify radial pressure jump distributions for a propulsor operating in boundary layer ingestion on a body of revolution that lead to reduced mixing losses in the slipstream, while still delivering the required thrust. These distributions should also be compatible with realistic propeller blade designs.

In physical terms the central quantity of interest is the non uniform axial velocity distribution in the slipstream of the body and actuator disk system. Strong radial gradients in this velocity distribution represent shear layers that will mix and dissipate kinetic energy. The aim is therefore to find radial pressure jump distributions that give a slipstream with smaller velocity differences between adjacent radii, particularly between the inner boundary layer region and the outer flow, without simply pushing the problem elsewhere or losing too much benefit from ingesting low momentum fluid.

To isolate this problem, the planned methodology involves two levels of formulation:

- At the actuator disk and slipstream level, for a fixed overall configuration and thrust requirement, identify radial pressure jump distributions that lead to reduced mixing loss and to a favourable distribution of power flux in the slipstream.
- At the blade level, for a given radial pressure jump distribution and inflow representation, design a propeller blade that can deliver that loading, and assess whether the resulting geometry and spanwise loading are reasonable.

In a formal sense this can be seen as an optimisation problem in which the radial pressure jump distribution is the main design input and the objective is to reduce a suitable measure of mixing loss or power dissipation in the slipstream, under constraints on thrust and on practical blade design. In this thesis the emphasis is on building and exercising the framework for such an optimisation rather than on running a specific numerical optimiser.

3.3.2. Design Variables

The preliminary methodology identifies several design variables and degrees of freedom that can be adjusted in order to explore the design space. The most important of these is the radial distribution of pressure jump across the actuator disk.

The radial pressure jump distribution $\Delta p(r)$ is controlled by a representation with multiple actuator disks at different radii. Each disk has a specified radius and produces a uniform pressure jump over its area. By selecting the number of disks, their radii and the fraction of total thrust assigned to each disk, a wide range of effective radial pressure jump distributions can be constructed. Examples include distributions that resemble an elliptical loading, distributions that concentrate thrust in the inner region or in the outer region, and distributions that keep the loading level inside the boundary layer low or high.

Additional design choices include

- the total thrust level that the actuator disk system must produce, which is linked to the assumed drag of the body and any other components in the configuration
- the representative boundary layer thickness and profile that define how the inflow to the disk varies with radius
- the selection of airfoil families and their distribution along the blade span in the inverse design framework
- the rotational speed and number of blades in the propeller design step.

In the strict sense not all of these are optimisation variables. Some are fixed to define a baseline configuration, while others are varied systematically to understand their influence on mixing loss and on the resulting blade designs. The key point is that the framework is built to treat the radial pressure jump distribution as a controllable design input rather than as a fixed assumption.

3.3.3. Constraints

The planned studies are subject to several physical and modelling constraints that shape the design space. These constraints ensure that the radial pressure jump distributions and the resulting blade designs remain meaningful for a boundary layer ingestion application.

The main constraints considered in the preliminary methodology are:

- **Thrust requirement.** For each configuration the total thrust produced by the actuator disk system must match a prescribed value representing the net drag of the body and any other components that are balanced by the propulsor at the chosen operating condition.
- **disk radius and geometry.** The outer radius of the actuator disk is fixed and is tied to the body size. The radial pressure jump distribution must therefore fit within this radius and must be compatible with the body geometry.
- **Pressure jump limits.** The pressure jump applied by the actuator disk should remain within a reasonable range so that the implied blade loading is not unrealistically high. In practice this means that very sharp peaks in $\Delta p(r)$ are avoided.
- **Flow quality.** The radial pressure jump distributions should not lead to flow features that clearly violate the assumptions of the low order model, such as extensive reverse flow at the disk or grossly separated slipstream structures.
- **Blade design practicality.** When a radial pressure jump distribution is passed to the inverse design framework, the resulting chord and twist distributions should be at least qualitatively rea-

sonable. Distributions that would require extremely large chord, very abrupt twist changes or highly oscillatory loading are viewed as impractical.

These constraints do not appear as explicit inequality constraints in a numerical optimiser in the present work. Instead they provide guidance on which families of radial loadings are worth considering and how the parameter space is to be explored.

3.3.4. Optimisation Loop Structure

Although no formal optimiser is implemented in this thesis, the preliminary methodology is based on the idea of an inner and outer loop structure that could support an optimisation in future work. This structure also helps to organise the modelling tasks.

The imagined inner loop consists of a flow and performance evaluation for a given choice of radial pressure jump distribution and other design inputs. It includes the following steps:

1. Define a candidate radial pressure jump distribution $\Delta p(r)$ using the multiple disk representation and fix the associated design inputs such as total thrust and boundary layer profile.
2. Run the axisymmetric flow model with body, boundary layer, actuator disk and slipstream representation to obtain the velocity field and the slipstream geometry for this candidate. This is an iteration loop where the upstream flow is also adjusted.
3. Compute slipstream based metrics such as mixing loss and power flux measures, as well as derived quantities such as power saving coefficient, following definitions that are introduced later in the thesis.
4. Pass the resulting radial pressure jump distribution to the inverse blade design model and derive the corresponding chord and twist distributions and three-dimensional propeller geometry.

The outer loop would then adjust the design inputs, primarily the radial pressure jump distribution, based on the outputs of the inner loop. In a true optimisation this could be driven by a numerical optimiser that seeks to reduce a scalar objective such as a mixing loss measure under constraints. In the planned methodology for this thesis the outer loop is instead realised as a structured exploration of a set of predefined radial loading families and parameter variations.

3.3.5. Optimisation Strategy

Given the complexity of the coupled flow and blade design problem and the limited time available for a master thesis, the chosen strategy is to focus on building a flexible framework and on exploring a discrete set of radial pressure jump distributions rather than implementing a fully automatic optimiser.

The planned optimisation strategy therefore consists of the following elements:

- Define a small number of radial loading families that are physically motivated. Examples include uniform loading, loading that approximates an elliptical distribution, and loadings that move thrust from the inner ingested region towards the outer region or vice versa.
- For each family vary a small set of parameters, such as the relative thrust assigned to different actuator disks, the radial break points between loading regions or the fraction of total thrust inside the boundary layer radius.
- For each candidate within this families and parameters space, run the inner loop described above to obtain mixing loss metrics, power flux information and inverse blade design results.

- Use the collection of results to identify trends and to discover which features of the radial pressure jump distribution appear favourable from the point of view of mixing loss and blade design.

In this sense the preliminary methodology treats optimisation in a broad sense, as the systematic search for better solutions, rather than as a formal problem for a specific algorithm. The framework is constructed in such a way that a more formal optimiser could be added in future work if desired.

3.3.6. Output

The expected output of the methodology can be grouped into three categories.

First, at the level of the body and actuator disk system, the framework delivers slipstream velocity fields, slipstream shapes and associated quantities such as mixing loss and power flux for each radial loading case that is considered. This allows different pressure jump distributions to be compared on a consistent basis.

Second, at the blade level, the inverse design model produces spanwise distributions of chord and twist and three dimensional propeller geometries corresponding to the radial loading cases. This shows how different disk level loadings translate into practical requirements for blade design and whether certain loadings would lead to unrealistic geometries.

Third, by combining these two levels the methodology yields qualitative design guidelines for boundary layer ingestion propulsors on bodies of revolution. In particular it provides insight into which types of radial pressure jump distribution offer a promising compromise between reduced mixing loss, reasonable propeller geometry and the desired thrust split between ingested and non-ingested flow.

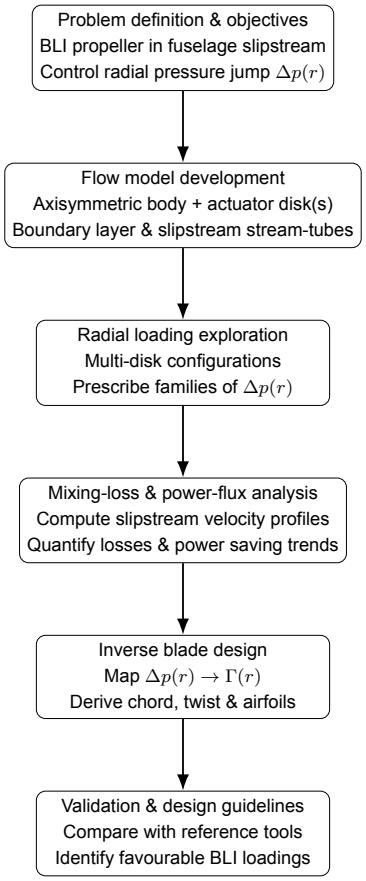

Figure 3.1: High-level methodology of the thesis: from problem definition, through development and use of an actuator-disk–based BLI flow model, to radial loading studies, inverse blade design and resulting design guidelines.

4

Coupled Actuator Disk Model

This chapter describes the coupled aerodynamic model used throughout this thesis to analyse boundary-layer ingestion (BLI) on an axisymmetric body of revolution. The framework combines a potential-flow solution for the outer flow, an integral boundary-layer model for the viscous region on the body, and an actuator-disk representation of the propulsor. The formulation and numerical approach are based on the potential-flow modelling framework developed by Kukučka [15], and are extended here with actuator-disk loading strategies (including multi-disk approximations of radial loading) and a slipstream correction model to provide the flow-field quantities required for the power-flux, mixing-loss and inverse blade-design analyses.

4.1. Physical Configuration and Model Assumptions

The configurations considered in this thesis consists of an axisymmetric body of revolution, representing a fuselage like shape, placed in a uniform free stream. One or more actuator disks are located at the trailing edge of the body, so that the disks ingest a part of the boundary layer created by the body.

The model is based on the following assumptions:

- steady, incompressible flow with constant density
- axisymmetry about the body axis
- inviscid outer flow, described using a velocity potential
- no swirl (the actuator disk is modelled as only creating a constant pressure jump, tangential forces are neglected)
- thin boundary layer on the body, described by integral boundary layer methods
- the actuator disk can be represented as an infinitesimally thin permeable surface with a prescribed jump in pressure
- the downstream slipstream can be represented by a set of concentric stream tubes whose radii and axial velocities evolve according to mass conservation.

Within these assumptions, the model provides a spatially resolved description of the axial and radial velocity field around the body and in the near slipstream of the actuator disk. This field is later used to compute power-flux and mixing-loss metrics and to drive the inverse blade design methodology.

4.2. Potential Flow Formulation

This section explains the potential flow formulation, which acts as the basis on which the rest of the model is built.

4.2.1. Governing Equation

Outside the boundary layer and away from the actuator disk, the flow is assumed inviscid and irrotational, so the velocity potential satisfies

$$\nabla^2 \phi = 0, \tag{4.1}$$

with $\mathbf{v} = \nabla\phi$. Equation (4.1) holds only in the fluid domain excluding the body and the disk. The solution is made unique by imposing boundary and jump conditions:

- **Impermeability on the body surface.** The body surface is treated as a streamline, so the normal velocity is set to zero at control points on S_{body}:

$$\nabla\phi \cdot \mathbf{n} = 0 \quad \text{on } S_{\text{body}}. \tag{4.2}$$

- **Prescribed loading at the actuator disk.** The actuator disk is modelled as an internal surface that imposes a specified pressure jump $\Delta p(r)$; this is enforced through a jump condition across the disk plane rather than by the Laplace equation.
- **Outer boundary condition.** The unbounded domain is approximated by a cylindrical boundary (tunnel wall or numerical far field) where the normal velocity is constrained to recover the desired far upstream behaviour and to prevent net mass flux through the boundary.

4.2.2. Body of Revolution representation

The body of revolution is defined by its meridional contour

$$r = r(x), \qquad x \in [x_{\min},\, x_{\max}]. \tag{4.3}$$

The contour is discretised into N axial segments with nodes (x_i, r_i). Control points are placed at segment midpoints,

$$x_{c,i} = \tfrac{1}{2}(x_i + x_{i+1}), \qquad r_{c,i} = \tfrac{1}{2}(r_i + r_{i+1}). \tag{4.4}$$

The local surface-normal direction is obtained from the segment slope,

$$\phi_i = \arctan\!\left(\frac{r_i - r_{i+1}}{x_{i+1} - x_i}\right), \qquad \hat{\mathbf{n}}_i = \sin\phi_i\, \hat{\mathbf{e}}_x + \cos\phi_i\, \hat{\mathbf{e}}_r. \tag{4.5}$$

The body is represented by axisymmetric source segments on the centreline. For segment j (length ℓ_j, strength σ_j), the induced velocity at (x, r) is

$$u_x = k_x\, \sigma_j, \qquad u_r = k_r\, \sigma_j, \tag{4.6}$$

with

$$k_x = \frac{1}{4\pi\, \ell_j\, r}\left(\sin\theta_2 - \sin\theta_1\right), \tag{4.7}$$

$$k_r = -\frac{1}{4\pi\, \ell_j\, r}\left(\cos\theta_2 - \cos\theta_1\right), \tag{4.8}$$

where θ_1, θ_2 are the angles from (x, r) to the two segment endpoints (at $x = x_j \mp \ell_j/2$).

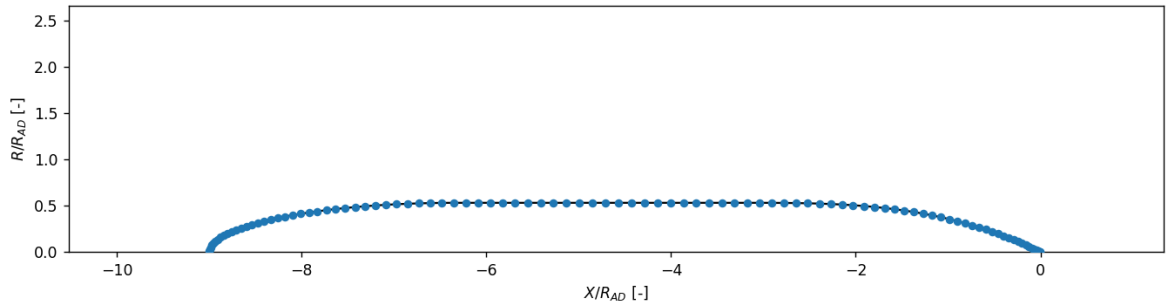

Figure 4.1: Body of revolution contour $r(x)$ and control points.

At each control point i,

$$\left(\mathbf{V}_\infty + \mathbf{u}_{\mathrm{AD}} + \mathbf{u}_{\mathrm{tunnel}} + \sum_{j=1}^{N_s} \mathbf{u}_j\right) \cdot \hat{\mathbf{n}}_i = 0, \tag{4.9}$$

which yields the linear system with entries

$$A_{ij} = k_x(x_{c,i}, r_{c,i}) \sin\phi_i + k_r(x_{c,i}, r_{c,i}) \cos\phi_i. \tag{4.10}$$

4.3. Actuator Disk Model implementation in Potential Flow

The actuator disk represents a propeller in a highly idealised manner. Instead of having individual blades, the actuator disk idealises a propeller as an infinitely thin, permeable surface across which the flow experiences a pressure jump. Usually, this pressure jump is constant in the radial direction. This pressure jump correspondingly influences an axial momentum change. For a given disk, the local thrust loading per unit area is given by:

$$t(r) = \Delta p(r) \tag{4.11}$$

Here, r represents the radius of the actuator disk.

Similarly, the total thrust can be calculated by integrating this over the entire radius:

$$T = 2\pi \int_0^{R_{\mathrm{disk}}} \Delta p(r)\, r \, \mathrm{d}r, \tag{4.12}$$

where R_{disk} is the disk radius.

4.3.1. Vorticity Representation and Induced Velocity

The pressure jump prescribed across the actuator disk is implemented through a vorticity-based representation of the added momentum in the slipstream. Within an inviscid potential-flow framework, the momentum addition associated with the disk is modelled by introducing vorticity rather than by directly modifying the velocity field.

The disk is discretised into a number of concentric annular elements. Each annulus sheds a circular vortex ring immediately downstream of the disk plane, with a circulation proportional to the local axial momentum addition across that annulus. The resulting set of vortex rings forms a discrete approximation of an axisymmetric vortex sheet convected downstream of the disk.

The induced velocity field is obtained by superposition of the contributions from all vortex rings. Analytical expressions for the velocity induced by a circular vortex ring are used to compute both the axial and radial velocity components. These induced velocities are added to the baseline potential-flow solution around the body, yielding a combined velocity field that satisfies the governing equations away from the disk and conserves the prescribed momentum addition in the slipstream.

Figure 4.2 shows the resulting streamline pattern of the coupled potential-flow and actuator-disk model, illustrating the slipstream development downstream of the disk location.

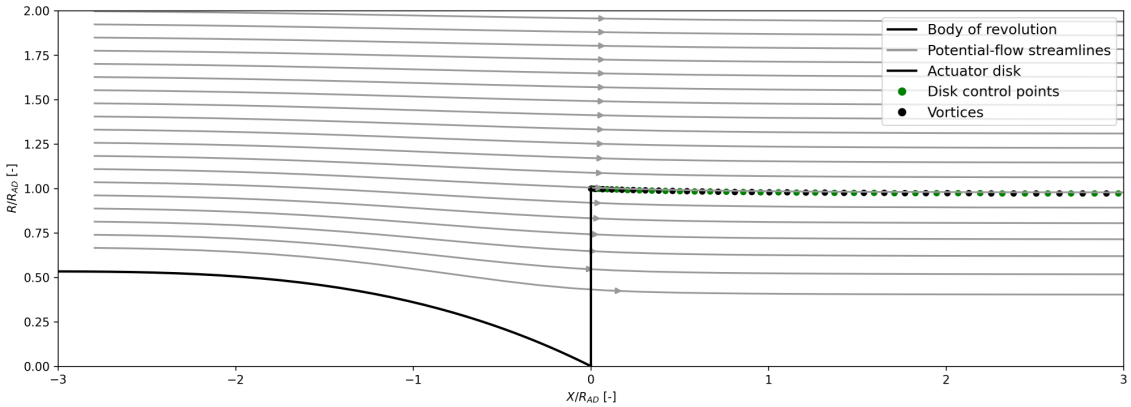

Figure 4.2: Coupled potential flow and actuator disk solution, showing the streamline pattern and slipstream contraction induced by the vorticity-based representation of the disk loading.

4.4. Boundary Layer Modelling

The presence of a fuselage boundary layer upstream of the propulsor is central to the boundary layer ingestion concept. In the present model, the boundary layer developing on the axisymmetric body of revolution is modelled using a low-order integral approach. Laminar and turbulent regions are treated separately, and axial symmetry and body curvature are accounted for through appropriate geometric factors. The model provides the evolution of boundary layer thickness, displacement thickness and momentum thickness along the body. These quantities are used both to update the effective outer body contour and to extract boundary-layer streamtubes that subsequently interact with the actuator disks and slipstream.

4.4.1. External velocity distribution and geometry

The boundary-layer model is solved along the meridional contour of the body of revolution, defined by stations $\{x_i, r_i\}$ and local surface angle $\phi(x)$. At each station the solution is described by displacement thickness $\delta_1(x)$, momentum thickness $\delta_2(x)$, and shape factor $H(x) = \delta_1/\delta_2$.

The driving outer-edge velocity $U_e(x)$ is taken from the coupled potential-flow solution. For each coupling iteration, U_e is evaluated on an offset contour outside the body, obtained by moving the surface outward along the local normal using the current boundary-layer thickness. In the first iteration, when

no boundary-layer thickness is available, $U_e(x)$ is approximated by interpolation of the surface velocity.

4.4.2. Laminar boundary layer

From the nose to a prescribed transition location, the boundary layer is assumed laminar and closed using the Blasius similarity solution [24]. The momentum thickness is advanced by the axisymmetric Kármán momentum–integral equation for a body of revolution [24]:

$$\frac{\mathrm{d}}{\mathrm{d}x}\left(r^2 \delta_2 U_e\right) + r\,\delta_2 \frac{\mathrm{d}U_e}{\mathrm{d}x} = \frac{\tau_w}{\rho U_e}. \tag{4.13}$$

The laminar wall shear is computed from the Blasius skin-friction law [6, 24]:

$$C_{f,\ell} = \frac{0.664}{\sqrt{\mathrm{Re}_x}}, \qquad \mathrm{Re}_x = \frac{U_e x}{\nu}, \qquad \tau_w = \tfrac{1}{2}\rho U_e^2 C_{f,\ell}. \tag{4.14}$$

The integral equation is discretised station-by-station as

$$\delta_{2,\ell}(x_i) = \delta_{2,\ell}(x_{i-1}) + \frac{\Delta x_i}{r_i^2 U_{e,i}}\left[\frac{\tau_{w,i}}{\rho U_{e,i}} - r_i\,\delta_{2,\ell}(x_{i-1})\frac{U_{e,i}-U_{e,i-1}}{\Delta x_i}\right], \tag{4.15}$$

with $\Delta x_i = x_i - x_{i-1}$.

For the Blasius profile, displacement thickness and boundary-layer thickness are obtained from fixed ratios to the momentum thickness [24]:

$$\delta_{1,\ell}(x_i) = 1.7208\,\delta_{2,\ell}(x_i), \tag{4.16}$$

$$\delta_{\ell}(x_i) = 4.913\,\delta_{2,\ell}(x_i), \tag{4.17}$$

giving the laminar shape factor $H_\ell = 2.59$. Figure 4.3 shows the velocity profile used for these relations.

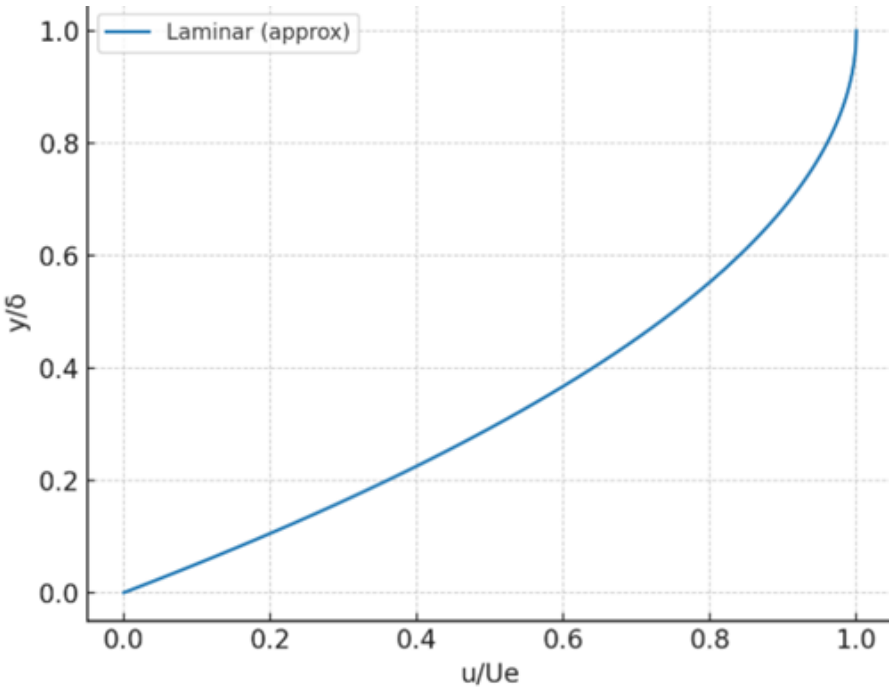

Figure 4.3: Blasius laminar boundary-layer velocity profile (u/U_e versus y/δ).

4.4.3. Turbulent boundary layer

Downstream of transition the boundary layer is assumed fully turbulent. A one–seventh power-law profile is used as a closure [24]:

$$\frac{u(y)}{U_e} = \left(\frac{y}{\delta_t}\right)^{1/7}, \qquad 0 \le y \le \delta_t. \tag{4.18}$$

Figure 4.4 shows this profile.

Direct integration of (4.18) gives

$$\delta_{1,t} = \frac{1}{8}\,\delta_t, \tag{4.19}$$

$$\delta_{2,t} = \frac{7}{72}\,\delta_t, \tag{4.20}$$

so the implied shape factor is constant: $H_t = \delta_{1,t}/\delta_{2,t} = 9/7$. The wall shear is closed with the standard flat-plate correlation consistent with the one–seventh law [24]:

$$C_{f,t}(x) = \frac{0.027}{\mathrm{Re}_x^{1/7}}, \qquad \tau_w = \tfrac{1}{2}\rho U_e^2 C_{f,t}. \tag{4.21}$$

The turbulent momentum thickness is advanced using the same axisymmetric integral form as in the laminar region [24]:

$$\delta_{2,t}(x_i) = \delta_{2,t}(x_{i-1}) + \frac{\Delta x_i}{r_i^2 U_{e,i}}\left[\frac{\tau_{w,i}}{\rho U_{e,i}} - r_i\,\delta_{2,t}(x_{i-1})\frac{U_{e,i} - U_{e,i-1}}{\Delta x_i}\right]. \tag{4.22}$$

Once $\delta_{2,t}(x_i)$ is known,

$$\delta_{1,t}(x_i) = H_t\,\delta_{2,t}(x_i), \qquad \delta_t(x_i) = \frac{72}{7}\,\delta_{2,t}(x_i). \tag{4.23}$$

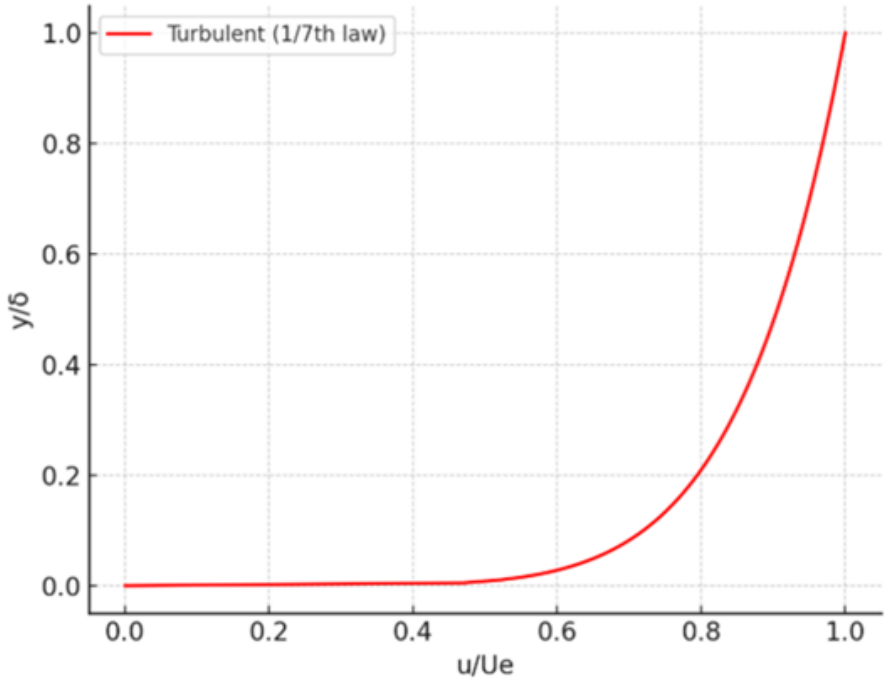

Figure 4.4: Turbulent boundary-layer velocity profile based on the one–seventh power law (u/U_e versus y/δ_t).

4.4.4. Transition, physical definitions and coupling

The transition location is prescribed as a fixed fraction of the body length. Upstream, $\{\delta_1, \delta_2, H, C_f\}$ are taken from the laminar model; downstream, from the turbulent model.

For coupling to the potential-flow solver, “physical” thicknesses are defined normal to the local surface by projecting the planar thicknesses using the local surface angle $\phi(x)$. The displacement thickness is used to form an effective outer body contour by offsetting the original surface along the outward normal. This contour is then used to update the outer inviscid flow and the next estimate of $U_e(x)$.

The boundary-layer edge also defines the initial conditions for the boundary-layer streamtubes used in the slipstream analysis. The combined effect of displacement and actuator-disk loading on the streamline field is shown in Fig. 4.5.

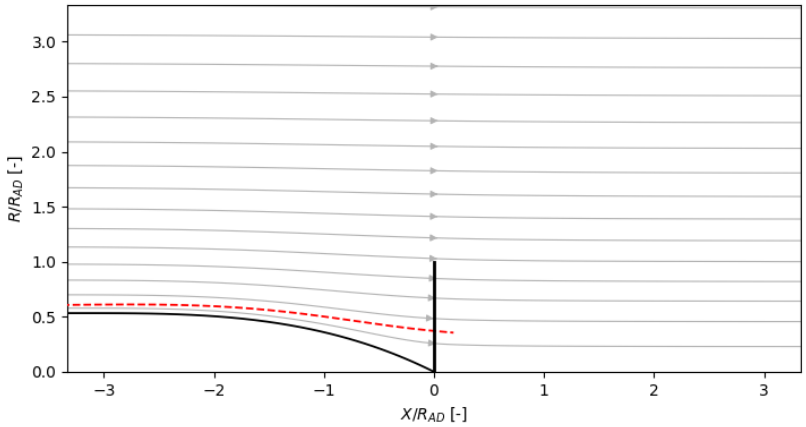

Figure 4.5: Coupled potential flow, boundary layer and actuator disk. The displacement thickness shifts the effective body contour, and the actuator disk accelerates the flow and contracts the slipstream.

4.5. Slipstream Correction Model

The actuator-disk model describes the loading at the propulsor but does not capture the downstream slipstream geometry resulting from the interaction between the propulsor, the body boundary layer, and the outer flow. Since this slipstream structure directly affects the evaluation of mixing losses, a low-order slipstream correction model is introduced.

4.5.1. Motivation

The actuator-disk model prescribes a radial pressure jump $\Delta p(r)$ and the associated acceleration of the flow through the disk, but does not describe the downstream slipstream geometry. In particular, radial redistribution of momentum and interaction with the body wake are not captured. Since these effects directly influence mixing losses and power fluxes, a slipstream correction model is introduced.

4.5.2. Slipstream model

The combined body–propulsor slipstream is represented using an axisymmetric streamtube model. The slipstream cross-section is discretised into concentric streamtubes, each carrying a fixed mass flow. For each streamtube j, mass conservation is enforced as

$$\dot{m}_j = \rho\, U_j(x)\, A_j(x) = \text{constant}, \tag{4.24}$$

allowing the streamtube radii to expand or contract in response to the local velocity field.

The slipstream is assumed to originate at the outer edge of the body boundary layer at the trailing edge. Initial streamtube properties are obtained by interpolating the boundary-layer solution at this location.

4.5.3. Coupling to the potential flow

Downstream of the slipstream origin, the streamtube radii are marched in the axial direction using velocities obtained from the coupled potential-flow solution. The resulting mass-flow deficit relative to the outer flow is expressed through a slipstream displacement thickness δ_{w}, defined such that

$$\dot{M}_{\mathrm{disp}} = \rho\, U_{\mathrm{out}}\, \pi\big(r_{\mathrm{edge}}^2 - (r_{\mathrm{edge}} - \delta_{\mathrm{w}})^2\big)\,. \tag{4.25}$$

The displacement thickness defines the effective slipstream boundary. Its local orientation is obtained from the slipstream radius distribution as

$$\theta_{\mathrm{w}}(x_i) = \arctan\left(\frac{r_{\mathrm{w}}(x_i) - r_{\mathrm{w}}(x_{i-1})}{x_i - x_{i-1}}\right). \tag{4.26}$$

Axisymmetric source elements are placed along this boundary to represent the displacement effect of the slipstream on the outer inviscid flow. The corrected slipstream velocities are subsequently used for the evaluation of mixing losses and power fluxes (Chapter 5).

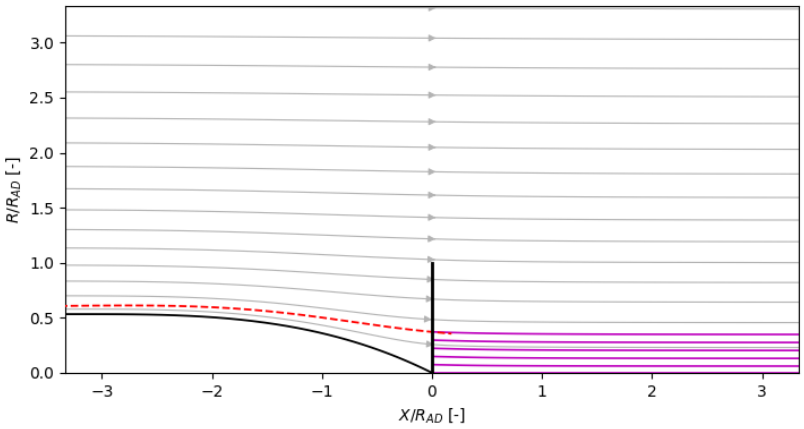

Figure 4.6: Fully coupled configuration including potential flow, boundary layer, actuator disk, and slipstream correction model. The redistribution of streamtubes downstream of the disk is illustrated.

4.6. From a single to multiple actuator disks

This section describes the methodology used in order to control the radial distribution of the pressure jump that is provided by the actuator disk. This is being done by adding multiple actuator disks of reducing radii one after the other.

4.6.1. Limitation of a single actuator disk

In its simplest form, the actuator disk in this model applies a *uniform* pressure jump over its entire area. Once the total thrust T and disk radius R_{disk} are specified, the mean pressure jump is fixed by

$$\Delta p = \frac{T}{A_{\mathrm{disk}}} = \frac{T}{\pi R_{\mathrm{disk}}^2}, \tag{4.27}$$

and this same Δp acts at all radii $0 \le r \le R_{\mathrm{disk}}$. In other words, in the single-disk formulation the model has no direct way to prescribe a radial variation $\Delta p(r)$: the disk is either “on” or “off”, and the only degrees of freedom are the total thrust and the overall size and position of the disk.

Some radial variation in induced velocity still appears because the inflow is non-uniform (due to the boundary layer) and because the disk has a finite radius. However, this variation is a consequence of the inflow and geometry, not a design choice in the loading. If one wishes to investigate how different *radial* pressure-jump distributions influence the slipstream structure and mixing loss, a single uniformly loaded disk is therefore too restrictive.

4.6.2. Motivation for multiple disks

A central aim of this work is to study and ultimately control the radial pressure-jump distribution $\Delta p(r)$. In an idealised uniform inflow, an approximately elliptical radial loading is known to minimise induced losses. In a boundary-layer-ingesting configuration, the optimal loading will not be exactly elliptical, but the same principle applies: the ability to place more or less pressure jump at specific radii is essential.

To gain this control in a simple and flexible way, the actuator surface is not kept as a single disk. Instead, it is decomposed into several coaxial actuator disks with different radii and thrust levels. Each of these disks acts on a specific radial band of the flow and can be given its own constant pressure jump. The superposition of all disks then produces an ***effective*** radial distribution $\Delta p_{\mathrm{eff}}(r)$ that is piecewise constant but can be shaped to resemble a desired continuous profile (such as an elliptical-like distribution adapted to BLI inflow).

4.6.3. Construction of the multi-disk system

The multi-disk configuration is constructed in three steps:

1. **Radial partitioning.** The overall propulsor radius R_{tot} is partitioned into radial bands. Each band is associated with one actuator disk. For example, an inner disk may extend up to a radius R_1, a second disk from R_1 to R_2, and an outer disk from R_2 to R_{tot}. In the axisymmetric model these bands are represented as disks with different radii, so that each disk predominantly affects "its" part of the inflow.
2. **Thrust allocation.** The prescribed total thrust T_{tot} is split into contributions T_i for each disk i using thrust fractions f_i:
$$T_i = f_i\, T_{\mathrm{tot}}, \qquad \sum_i f_i = 1. \tag{4.28}$$
For a disk of area $A_i = \pi R_i^2$, this gives a mean pressure jump on that disk of
$$\Delta p_i = \frac{T_i}{A_i}. \tag{4.29}$$
Because A_i and T_i can differ between disks, the resulting Δp_i will also differ. By choosing the radii R_i and the fractions f_i, the effective $\Delta p_{\mathrm{eff}}(r)$ becomes a piecewise distribution: higher in some radial bands, lower in others.
3. **Axial spacing.** The individual disks are placed at slightly different axial positions, separated by small gaps. Physically, this allows the flow accelerated by an upstream disk to adjust before encountering the next one, and it avoids numerical singularities associated with placing multiple pressure jumps exactly in the same plane. From a modelling point of view, the propulsor still behaves as a single system, but the induced velocity field is smoother than if all jumps were applied in a single plane.

4.6.4. Multi-disk loading versus elliptical distribution

To evaluate how well a finite number of concentric actuator disks can represent a smooth radial loading, the one-disk, two-disk and four-disk configurations are compared to an idealised elliptical distribution.

The ellipse is taken as the target bell-shaped loading profile $y_{\mathrm{ell}}(r)$, while the actuator-disk configurations are represented by stacked rectangles $y_{\mathrm{rect}}(r)$ of constant height over prescribed radial intervals (see Fig. 4.7). For each case, the total area under the rectangular profile is scaled to match the area under the ellipse, so that the integral thrust is essentially the same. The remaining question is how well the *shape* of the radial loading is reproduced.

The similarity between the rectangular approximation and the elliptical reference is quantified using a relative L_2 shape error. Denoting the outer radius by R, the error is defined as

$$\varepsilon_{L_2} = \frac{\left(\int_0^R \left[y_{\mathrm{rect}}(r) - y_{\mathrm{ell}}(r) \right]^2 \mathrm{d}r \right)^{1/2}}{\left(\int_0^R y_{\mathrm{ell}}^2(r)\, \mathrm{d}r \right)^{1/2}}, \tag{4.30}$$

which measures the root-mean-square deviation between the two curves, normalised by the rms level of the reference ellipse.

For a single uniformly loaded disk, the relative L_2 shape error is approximately 31%, indicating that the constant radial loading is a poor representation of the bell-shaped elliptical profile. Allowing two disks, and therefore two different constant loading levels over an inner and an outer band, already improves the fit: the error drops to about 18%. With four disks, the rectangular bands become narrower and their heights can vary more gradually across the radius. This additional flexibility reduces the error further to roughly 9%. The trend is clearly visible in Fig. 4.7: as the number of disks increases, the stacked rectangles trace the curvature of the ellipse more closely.

In summary, the L_2 shape error confirms that increasing the number of concentric actuator disks does not change the total thrust, but it does lead to a progressively better representation of the desired elliptical radial distribution. This improved shape fidelity is important for the subsequent slipstream calculations and mixing-loss analysis, where the radial variation of the pressure jump is more relevant than the exact value of the integral thrust alone.

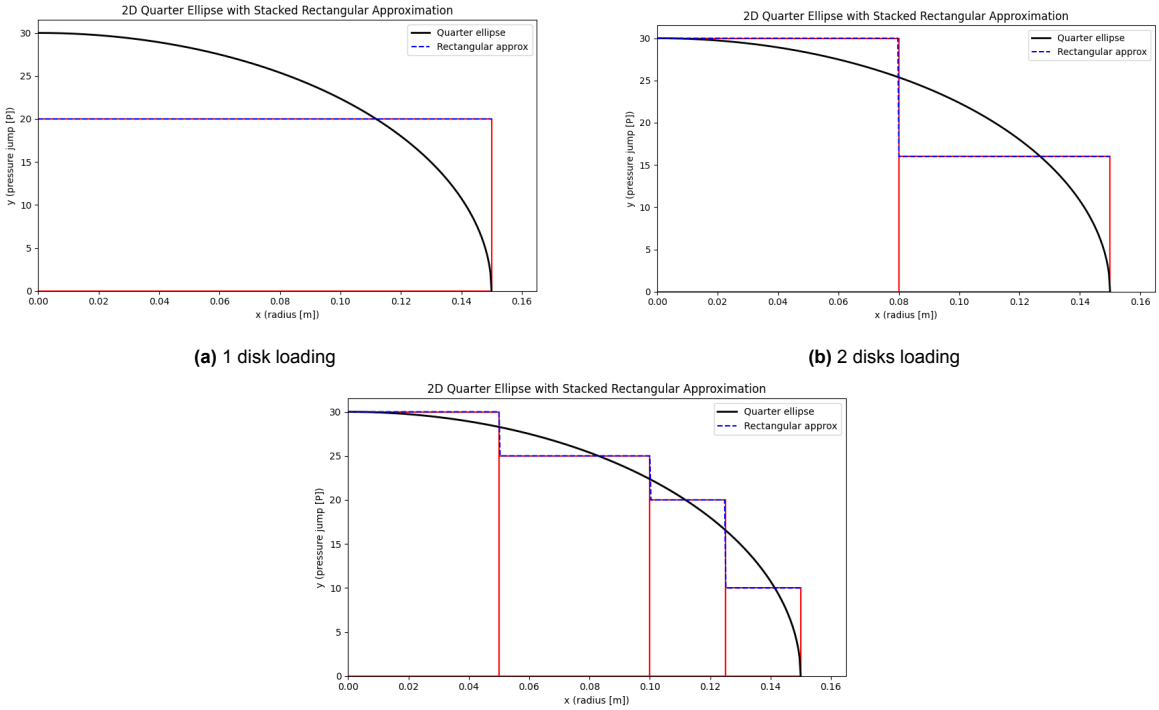

(a) 1 disk loading

(b) 2 disks loading

(c) 4 disk loading

Figure 4.7: Radial loading representations for actuator-disk configurations with one, two and four concentric disks. The rectangles are scaled to match the total area of the reference elliptical distribution, while the L_2 shape error (4.30) quantifies the remaining difference in radial shape.

With four actuator disks, the fully coupled model is shown in Fig. 4.8. The four black bars near $x = 0\,\mathrm{m}$ represent the individual actuator disks, placed one after the other with a prescribed axial spacing and with different radii. The smallest disk is chosen to be slightly larger than the slipstream radius used in the wake model. This ensures that the coupling between the actuator-disk solver and the slipstream model remains robust, as the current implementation does not yet support a radially varying pressure jump that is entirely confined within the slipstream region.

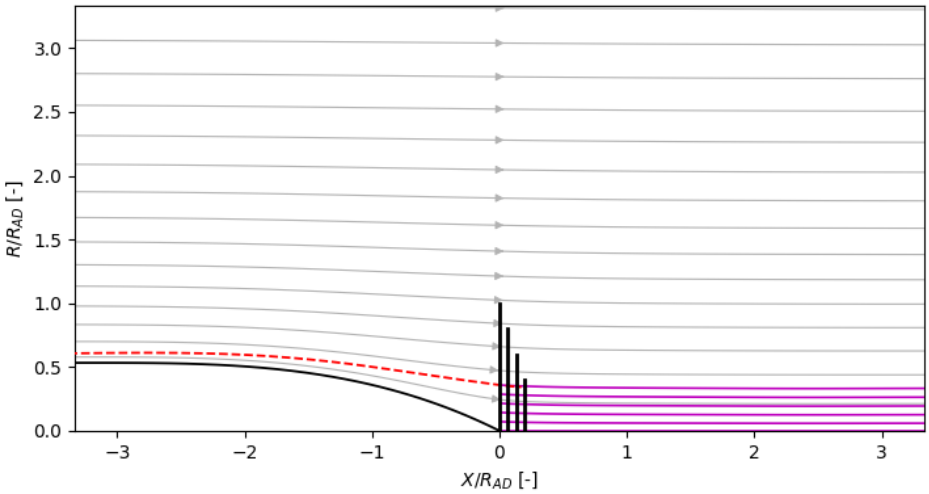

Figure 4.8: Combined coupled model with four actuator disks, illustrating the concentric loading bands used to approximate the elliptical target distribution.

4.7. Numerical solution procedure

In this section, the numerical procedure used to solve the coupled body, actuator disk, and boundary layer problem is summarized. The main steps of the algorithm are shown in Figure 4.9. The procedure starts with the definition of the problem parameters and the creation of the objects that represent the body, actuator disks, and boundary layer. An initial linear solve with a prescribed thrust provides a first estimate of the flow field.

The core of the method is an iterative loop in which the slipstream radius, the boundary layer solution and the slipstream correction are updated, after which drag and net force are evaluated and the thrust is adjusted to enforce force balance. Once the convergence check is satisfied, a post processing stage computes the final drag and thrust, mixing losses and power flux, and saves the results and plots.

The convergence check is done by caluclating the reation between the provided thrust by the combination of actuator disks and the calculated skin friction drag due to the body of revolution. The solution is converged once these 2 values are equal to each other.

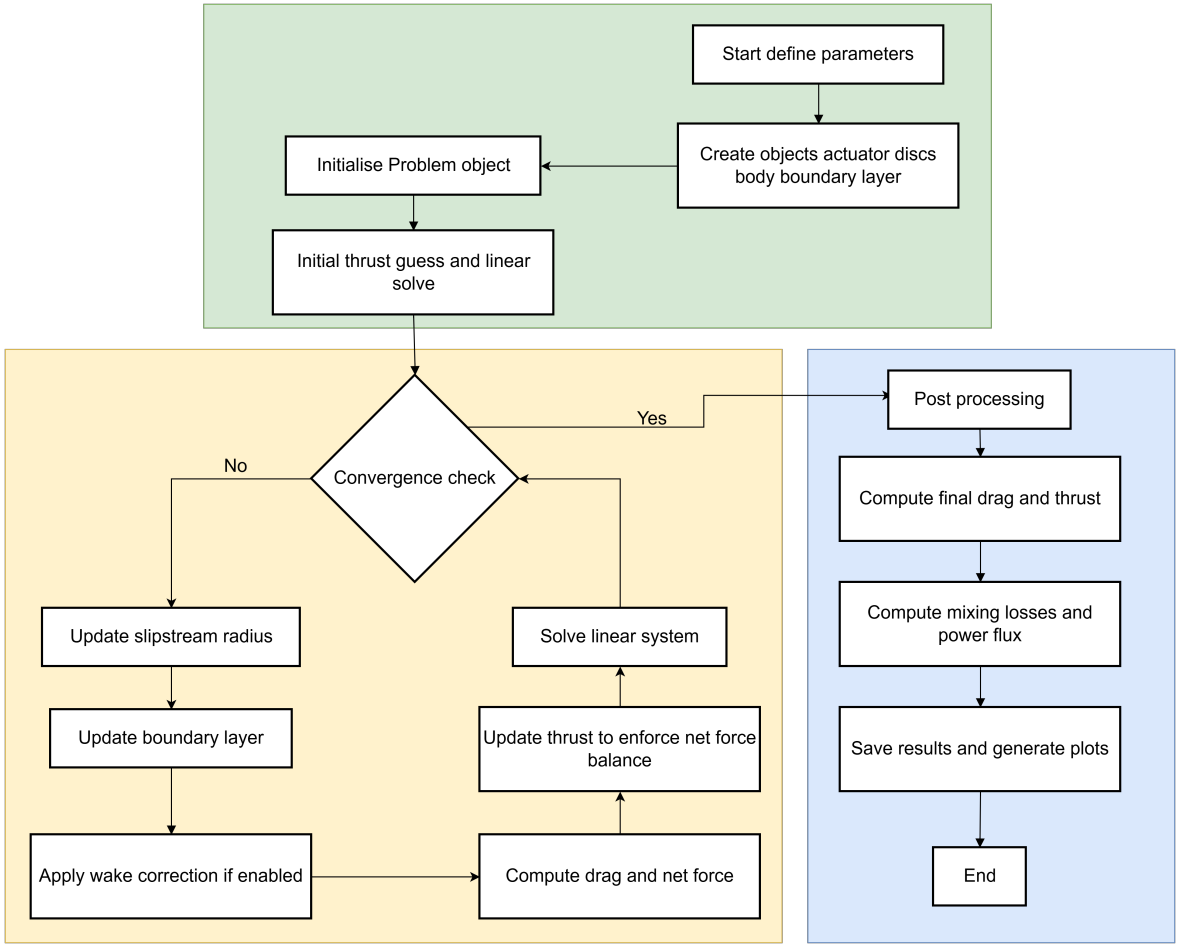

Figure 4.9: Coupled Actuator Disk Model Flow

4.8. Results of the coupled model

This section illustrates the behavior of the fully coupled model, in which the potential flow solution, the body boundary layer, and the slipstream correction are all active. The focus is on two representative configurations. The first is the baseline with a single actuator disk. The second is a configuration with four actuator disks that is used to approximate an elliptical pressure jump distribution in radius.

4.8.1. Single actuator disk

The starting point of the analysis is the baseline configuration with a single actuator disk at the axial location of the propulsor. Figure 4.10 shows the coupled flow field for this case. The body, the boundary layer and the actuator disk are all visible, together with streamlines and slipstream streamtubes.

Upstream of the disk the boundary layer develops along the body and produces a slipstream deficit behind the trailing edge. The streamlines near the wall are displaced away from the body due to the displacement thickness that is imposed on the potential flow. This creates a thicker slipstream region in which the axial velocity is reduced compared to the free stream.

Across the disk the prescribed pressure jump accelerates the flow in the loaded annulus. This is seen as a local contraction of the streamlines and an increase in axial velocity downstream of the disk plane. The slipstream edge appears as a shear layer that separates the accelerated core from the outer flow

that is only weakly disturbed by the propulsor.

Further downstream the slipstream correction model redistributes the mass flow over concentric streamtubes. The slipstream streamtubes expand and gradually relax, and the axial velocity in the slipstream core approaches a nearly constant value. The combination of body boundary layer, actuator disk loading and slipstream expansion gives a first impression of how the coupled model represents a boundary layer ingestion propulsor.

4.8.2. Four actuator disks

The second configuration employs four actuator disks of different radii, placed with a small axial spacing. This arrangement is used to approximate an elliptical radial pressure-jump distribution, in which the loading is concentrated towards the inner part of the slipstream and gradually reduced towards the outer radius. The disk radii are chosen as $R = 0.15$ m, $0.8R$, $0.6R$, and $0.4R$, respectively. Each actuator disk is prescribed the same thrust per unit area, such that the overall radial loading distribution is determined solely by the disk radii rather than by differences in local disk strength.

Figure 4.11 shows the axial velocity field for this configuration, normalised by the free-stream velocity. The superposition of the four loading planes produces a radially non-uniform acceleration of the flow, with the strongest velocity increase occurring near the axis and a smoother transition towards the slipstream edge. This behaviour reflects the intended elliptical loading, in which low-momentum fluid from the boundary layer is preferentially re-energised while avoiding excessive acceleration near the slipstream boundary.

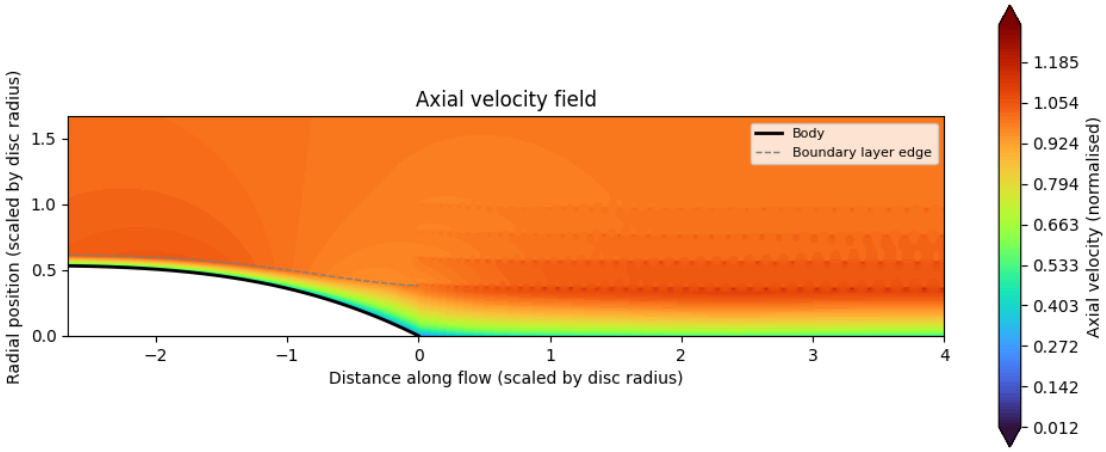

Figure 4.11: Normalised axial velocity field V_x/V_∞ for the fully coupled model with four actuator disks of radii 0.15 m, 0.12 m, 0.09 m, and 0.06 m.

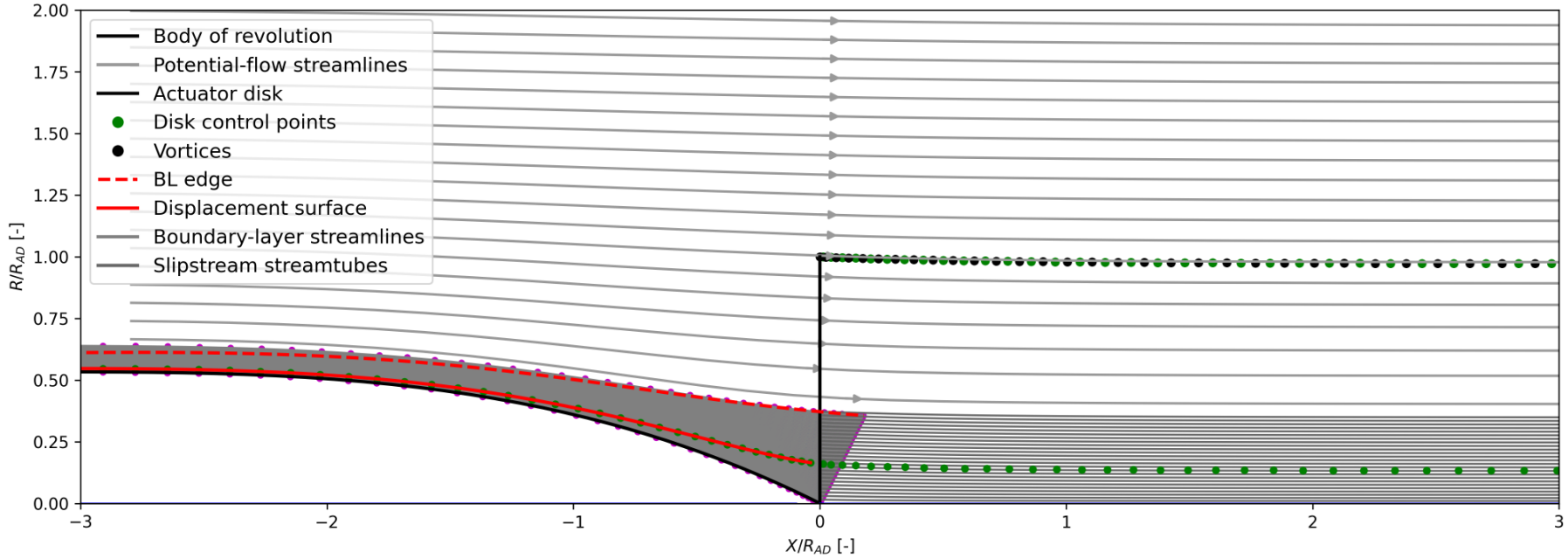

Figure 4.10: Flow field of the fully coupled model for the single actuator disk configuration. Streamlines and slipstream streamtubes are shown together with the body and the disk location.

5

Mixing Loss and Power Flux Analysis

The actuator-disk boundary layer ingestion model developed in the previous chapter provides the velocity field in the slipstream of the body and propulsor. To compare radial loading strategies and relate slipstream behaviour to propulsive performance, this chapter introduces two scalar measures:

- an axisymmetric mixing-loss metric based on radial shear in the axial velocity, and
- power-flux measures that quantify how much kinetic energy is added to and carried by the slipstream.

Both measures are simple by design. They do not replace turbulence modelling or a full exergy balance, but provide a consistent way to compare radial pressure-jump distributions within the low-order framework of this thesis.

5.1. Motivation and definitions

In a boundary layer ingestion configuration, the propulsor ingests low-mo mentum fluid from the body wake and accelerates it. Ideally, the slipstream velocity should be uniform in radius so that no further irreversible mixing is required and the available kinetic energy is used efficiently. In practice, the body, actuator disk and finite number of blades produce non-uniform velocity distributions in radius and in the axial direction.

Mixing losses are associated with velocity gradients that drive shear and turbulence. In the axisymmetric model used here, the relevant gradients are the radial variations of the axial velocity component in the slipstream. Strong radial gradients in $V_x(r)$ at a given axial station indicate shear layers that will generate turbulence and dissipate kinetic energy downstream.

At the same time, the propulsor adds kinetic energy to the flow to produce thrust. The rate at which kinetic energy is transported downstream by the slipstream is interpreted as a power flux. Comparing power fluxes between configurations, and between cross sections before and after the propulsor, shows how the supplied power is distributed between useful thrust and slipstream kinetic energy.

Both the mixing loss and power flux evaluations are performed at a downstream distance of approximately $0.5\ \mathrm{m}$ from the actuator disk. This choice follows from the observed development of the axial velocity in the slipstream, where the flow requires roughly three actuator disk radii to reach a quasi

steady state after passing through the propulsor.

The evolution of the streamline velocities for the four disk configuration is shown in Figure 5.1. The axial velocity continues to increase over the first several tenths of a metre downstream and stabilises only beyond $x \approx 0.5$ m. The streamline originating inside the boundary layer experiences the largest acceleration, which is consistent with the fact that the strongest pressure jump is applied in this region. For this reason the location $x = 0.5$ m is used as the representative downstream plane for the comparison of mixing loss and power flux results across all actuator disk configurations.

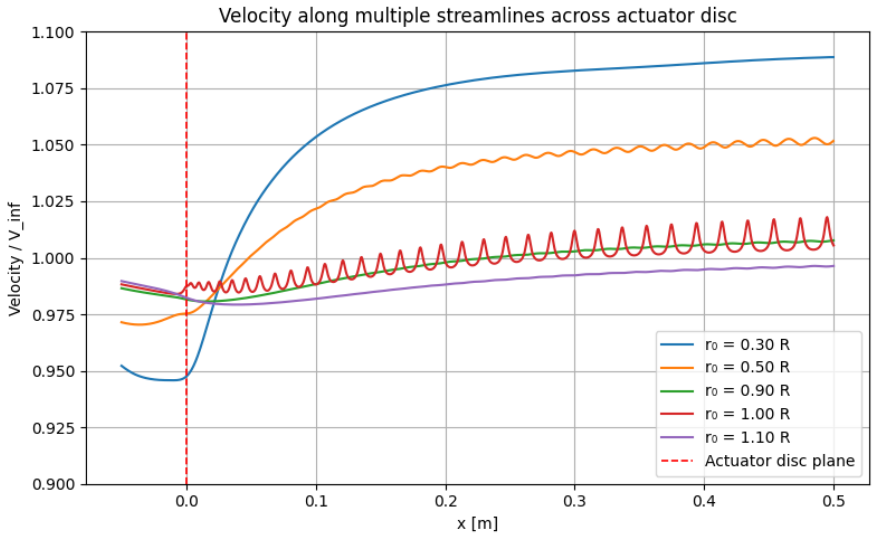

Figure 5.1: Streamline evolution of model with 4 actuator disks

5.2. Axisymmetric mixing-loss metric

5.2.1. Definition

The mixing-loss metric is based on the radial shear of the axial velocity in a cross section of the slipstream. For a given axial location x, the model evaluates the axial velocity $V_x(r)$ on a radial line and estimates its radial derivative $\partial V_x/\partial r$. Stronger radial gradients correspond to stronger shear and higher mixing loss.

An axisymmetric proxy for the rate at which viscous effects dissipate energy is

$$P_{\text{mix}}(x) = 2\pi\mu \int_0^{r_{\max}} \left(\frac{\partial V_x}{\partial r}(x, r)\right)^2 r \, \mathrm{d}r, \tag{5.1}$$

where μ is the dynamic viscosity of air and $r_{\max}$ is chosen to cover the slipstream region of interest. The factor $2\pi\mu$ corresponds to circumferential integration of a quantity proportional to $(\partial V_x/\partial r)^2$ over a ring at radius r. The quantity $P_{\text{mix}}(x)$ has the dimensions of power per unit axial length and is used as a mixing-loss metric for that axial station.

Within this work the analysis focuses on relative comparisons between configurations and axial positions. The absolute value of P_{mix} is less important than its variation with x and its sensitivity to changes in the radial pressure-jump distribution.

5.2.2. Combined velocity field and axial averaging

In the numerical implementation the velocity field used in Equation (5.1) is built from two components:

- a potential-flow solution, which provides induced axial and radial velocities $(V_{x,\text{pot}}, V_{r,\text{pot}})$ everywhere, and
- a slipstream model for the actuator disk, which provides piecewise constant axial velocities along streamtubes in the propulsor slipstream.

The axial velocity used in the mixing-loss evaluation combines these two fields:

- V_x is taken from the slipstream model where slipstream data are available and from the potential flow otherwise;
- V_r is always taken from the potential-flow solution.

This ensures that the mixing-loss metric reflects the axial velocity structure produced by the slipstream-correction model in the propulsor jet, without superposing two different representations of the same slipstream.

To reduce sensitivity to discrete slipstream structures, the velocity profile at a given axial location x is obtained by averaging over a small axial window centred on x. A set of locations $x \in [x - \Delta x, x + \Delta x]$ is defined and the profiles $V_x(x, r)$ on a radial grid are averaged over these sample points. The window half-width is of the order of one vortex spacing in the slipstream. This axial averaging smooths small-scale oscillations and yields a more robust estimate of the radial shear.

5.2.3. Numerical evaluation

For each axial station x where the mixing-loss metric is evaluated, the following steps are carried out:

1. Define a radial grid r_j between a small inner radius and $r_{\max}$, typically up to a factor of the actuator-disk radius.
2. Define an axial averaging window centred on x with half-width equal to a reference spacing between slipstream vortex elements, and choose a small number of sample points x_k in this window.
3. For each pair (x_k, r_j), compute the axial and radial velocities. Obtain the base values $(V_{x,\text{pot}}, V_{r,\text{pot}})$ from the potential-flow solution. If the point lies within the axial extent of the slipstream model and within a slipstream streamtube, override the axial velocity by the corresponding slipstream-model value; keep the radial velocity equal to the potential-flow value.
4. Average the axial velocity profiles over the sample points x_k to obtain a smoothed profile $V_x(x, r_j)$.
5. Approximate the radial derivative $\partial V_x/\partial r$ on this radial grid with a finite-difference gradient.
6. Evaluate the integrand $(\partial V_x/\partial r)^2 r$ at each radial grid point and compute the integral in Equation (5.1) using the trapezoidal rule.

The result is recorded as $P_{\text{mix}}(x)$. In the comparison studies this procedure is repeated for multiple axial locations downstream of the actuator disk for each radial loading case, and the resulting curves $P_{\text{mix}}(x)$ are compared between cases.

The mixing-loss metric is a simplified representation: it neglects detailed turbulence modelling and small-scale structure, but captures the effect that strong radial velocity gradients in the slipstream are associated with higher dissipation and provides a consistent way to compare radial loading strategies.

5.3. Power-flux analysis

This section defines the power-flux measures used in the analysis and introduces the normalised quantities used to present the results. Power flux is evaluated at three axial stations: (i) a freestream refer-

ence, (ii) an upstream plane representing the ingested boundary-layer inflow, and (iii) a downstream plane in the slipstream where the wake has developed. The locations used in the present framework are shown in Figure 5.2.

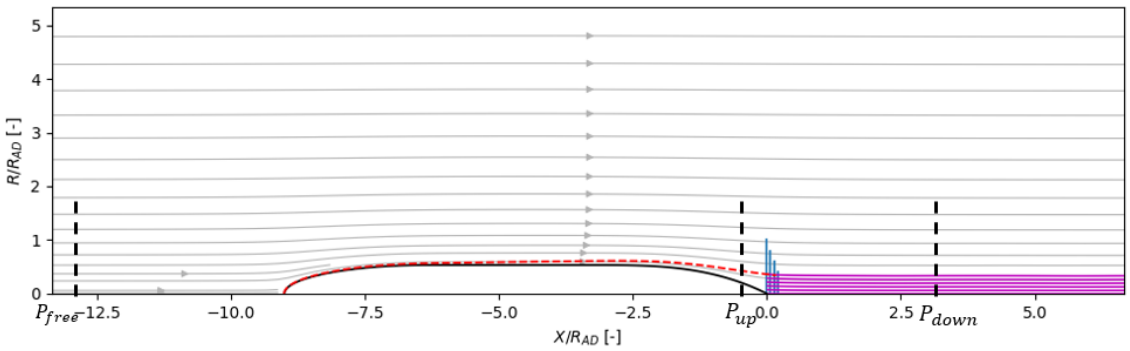

Figure 5.2: Axial stations used for power-flux evaluation: a freestream reference, an upstream plane, and a downstream plane.

5.3.1. Definition of power flux

For an incompressible flow, the kinetic power transported through a cross section at axial position x is defined as

$$\dot{P}(x) = \int_A \frac{1}{2}\,\rho\,V_x^3(x,r)\,\mathrm{d}A = \int_{r_{\min}}^{r_{\max}} \frac{1}{2}\,\rho\,V_x^3(x,r)\,2\pi r\,\mathrm{d}r, \tag{5.2}$$

where $V_x(x,r)$ is the axial velocity, ρ is the density, and $[r_{\min},\, r_{\max}]$ defines the annulus of interest. This quantity has the dimensions of power and represents the kinetic-energy flux through the control surface.

Within the present framework, the powered configuration corresponds to the flow past the body with its boundary layer and the actuator disk active. The corresponding power flux is denoted $P_{\text{body+disk}}(x)$ and is evaluated from the combined potential-flow and slipstream-corrected velocity field on the same radial grid used for thrust and mixing-loss calculations.

Freestream reference. A reference power flux is defined from a uniform freestream without body or disk:

$$P_\infty = \int_A \frac{1}{2}\,\rho\,V_\infty^3\,\mathrm{d}A = \frac{1}{2}\,\rho\,V_\infty^3\,\pi\left(r_{\max}^2 - r_{\min}^2\right), \tag{5.3}$$

where V_∞ is the freestream speed. This reference represents the kinetic power that would be present in an undisturbed flow through the same annulus.

Upstream plane. In the upstream plane, the inflow is affected by the body-induced boundary layer, resulting in a non-uniform axial velocity. In addition, the body induces a static-pressure field that contributes to the mechanical power flux through pressure work. The upstream power flux is therefore evaluated as

$$P_{\text{up}} = \int_A \left(\frac{1}{2}\,\rho\,V_x^3 + p\,V_x\right)\,\mathrm{d}A = \int_{r_{\min}}^{r_{\max}} \left(\frac{1}{2}\,\rho\,V_x^3(x,r) + p(x,r)\,V_x(x,r)\right)\,2\pi r\,\mathrm{d}r, \tag{5.4}$$

where $V_x(x,r)$ is the axial velocity from the boundary-layer model and $p(x,r)$ is the static pressure obtained from the potential-flow solution for the body without actuator forcing. The static pressure is assumed uniform across the boundary-layer thickness at a given radial location, such that the pressure field is fully determined by the outer potential flow.

Downstream plane. Downstream of the actuator disk, the axial velocity field is taken from the combined potential-flow and slipstream-corrected solution. The downstream power flux is evaluated using Equation 5.2 on the same annulus $[r_{\min}, r_{\max}]$, and is denoted P_{down}. This quantity captures the kinetic-energy flux remaining in the developed slipstream and is used as an indicator of wake non-uniformity and loss-related behaviour in the subsequent analysis.

5.3.2. Normalised power differences

In the numerical post-processing, the power-flux differences are expressed in dimensionless form. For a given configuration the upstream and downstream power fluxes in the powered case are

$$P_{\text{up}} = P_{\text{body+disk}}(x_{\text{up}}), \qquad P_{\text{down}} = P_{\text{body+disk}}(x_{\text{down}}), \tag{5.5}$$

evaluated at fixed axial positions upstream and downstream of the actuator disk.

Two normalised power differences are then formed:

$$\widehat{\Delta P}_{\text{down-up}} = \frac{P_{\text{down}} - P_{\text{up}}}{P_{\text{up}}}, \tag{5.6}$$

$$\widehat{\Delta P}_{\text{down-free}} = \frac{P_{\text{down}} - P_{\infty}}{P_{\infty}}. \tag{5.7}$$

The quantity $\widehat{\Delta P}_{\text{down-up}}$ measures the relative power added by the actuator system between the inlet boundary layer and the downstream plane, normalised by the upstream power flux in the annulus. The quantity $\widehat{\Delta P}_{\text{down-free}}$ measures the relative excess (or deficit) of downstream kinetic power flux with respect to a clean tunnel, normalised by the freestream reference P_{∞}. Both are reported as percentages in the results.

In the remainder of this chapter the shorthand

$$P(x) \equiv P_{\text{body+disk}}(x)$$

is used, and the focus is on the normalised differences $\widehat{\Delta P}_{\text{down-up}}$ and $\widehat{\Delta P}_{\text{down-free}}$ rather than on the absolute power levels in watts.

5.4. Results: mixing loss

The mixing-loss behaviour is analysed at a downstream station where the slipstream has stabilised. From the streamline plot in section 5.1 it is observed that the axial velocity in the slipstream becomes nearly constant at approximately $x \approx 0.5\ \text{m}$. The station $x = 0.5\ \text{m}$ is used as the reference location.

At this location, the radial structure of the slipstream is characterised by the axial velocity gradient $\partial V_x/\partial r$. The gradient is computed from the combined potential-flow and slipstream-corrected velocity field. The axial velocity is sampled on a radial grid at the x-positions of the vortex rings and then averaged over a small axial window to reduce local oscillations. The radial gradient is obtained from this averaged profile.

Figure 5.3 shows the normalised radial distributions of $\partial V_x/\partial r$ at $x = 0.5\ \text{m}$ for one to four actuator disks at equal total thrust. In the single-disk case (Figure 5.3a), the gradient exhibits a pronounced peak near the slipstream edge, indicating an abrupt velocity change between the slipstream core and the outer flow. When additional disks are introduced (Figures 5.3b–5.3d), the peak is reduced and the profile becomes progressively smoother. This reflects that the effective loading becomes more distributed, and approaches a more elliptical pressure-jump distribution, which yields a more gentle and less abrupt velocity gradient.

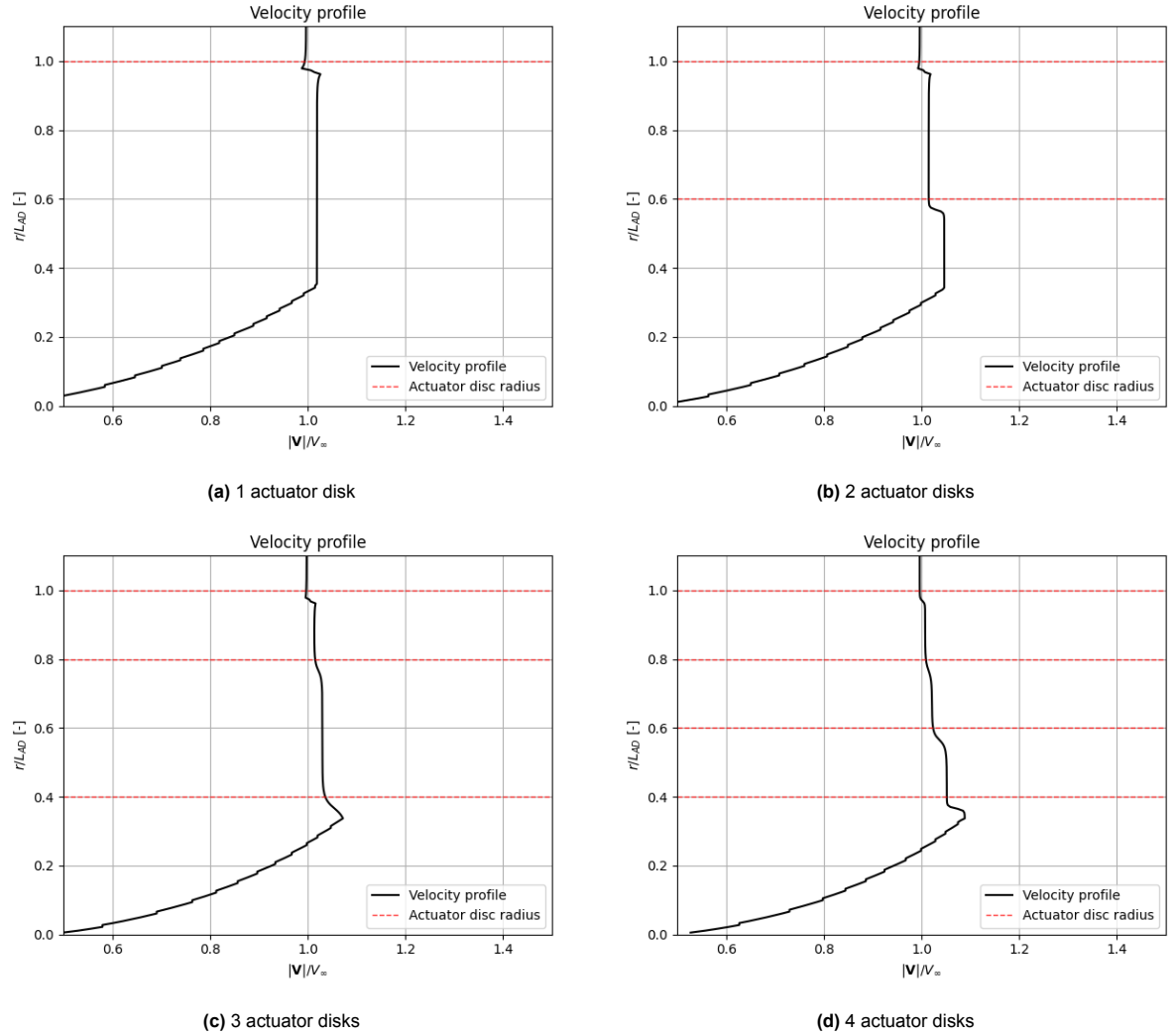

(a) 1 actuator disk

(b) 2 actuator disks

(c) 3 actuator disks

(d) 4 actuator disks

Figure 5.3: Normalised radial distributions of the axial velocity gradient $\partial V_x/\partial r$ at $x = 0.5$ m for configurations with one to four actuator disks at equal total thrust.

The integrated mixing-loss values are reported in Table 5.1. All cases produce the same total thrust. The values are normalised with respect to the single-disk case, with $L_{\mathrm{mix},1} = 0.01228$ W/m, such that $\tilde{L}_{\mathrm{mix},N} = L_{\mathrm{mix},N}/L_{\mathrm{mix},1}$. The normalised mixing loss decreases with the number of disks: $\tilde{L}_{\mathrm{mix},2} = 0.775$, $\tilde{L}_{\mathrm{mix},3} = 0.622$, and $\tilde{L}_{\mathrm{mix},4} = 0.558$. This trend follows from the mixing-loss integral scaling with $(\partial V_x/\partial r)^2$: smoothing the velocity gradient lowers the peak gradients and reduces the total loss.

Table 5.1: Mixing Loss. Values for $N > 1$ are normalised by the single-disk case $L_{\mathrm{mix},1} = 0.01228$ W/m.

Configuration	Normalised mixing loss $\tilde{L}_{\mathrm{mix}}$
1 disk	1.000
2 disks	0.775
3 disks	0.622
4 disks	0.558

5.5. Results: power-flux analysis

Two sets of power-flux results are compared. The first varies the number of actuator disks from one to four while keeping the overall loading concept fixed, showing how redistributing the same nominal thrust over more disks changes the downstream power flux and recovery of the ingested boundary layer. The second varies the radial thrust distribution for a fixed three-disk configuration, starting from approximately uniform thrust per unit area and progressively biasing the loading towards the inner radii where the inflow is most affected by the boundary layer.

All power-flux quantities are evaluated at a single upstream plane located $0.15\ \mathrm{m}$ upstream of the actuator disk and a downstream plane located $0.5\ \mathrm{m}$ behind it. For all configurations, the axial power flux has reached an approximately constant level at these distances. The results are presented in terms of the normalised differences $\widehat{\Delta P}_{\text{down-up}}$ and $\widehat{\Delta P}_{\text{down-free}}$ defined in Equations (5.6)–(5.7).

5.5.1. Number of actuator disks

In this subsection, only the number of actuator disks is varied, while the operating condition and thrust distribution per unit area are kept constant. Table 5.2 summarises the normalised power-flux differences for the four configurations considered.

Table 5.2: Normalised power-flux differences when only the number of actuator disks is varied.

Configuration	$\widehat{\Delta P}_{\mathrm{down-up}}$ [-]
1 disk	0.573
2 disks	0.550
3 disks	0.509
4 disks	0.501

All configurations introduce a significant increase in kinetic power between the inlet boundary layer and the downstream plane. The quantity $\widehat{\Delta P}_{\mathrm{down-up}}$ represents the additional power that must be supplied by the actuator system, normalised by the upstream power flux in the annulus.

When moving from a single-disk configuration to multi-disk layouts, the normalised upstream–downstream power-flux difference decreases monotonically from approximately 0.57 for one disk to about 0.50 for the three- and four-disk configurations. This indicates that, for effectively the same thrust level, distributing the pressure jump over multiple actuator disks reduces the fraction of the processed power that must be added between the two planes.

An additional contributing factor to this trend is the increased interaction between the actuator system and the inlet boundary layer as the number of disks increases. By distributing the pressure jump over multiple axial locations, a larger portion of the total power addition occurs closer to the low-momentum boundary-layer flow. As a result, the actuator system more effectively exploits the reduced kinetic energy of the ingested flow, leading to a lower relative power requirement for a given thrust level.

It can therefore be concluded that, for a fixed thrust level, increasing the number of actuator disks reduces the relative power requirement of the actuator system, indicating a more power-efficient propulsor configuration.

5.5.2. Effect of thrust weighting for the three-disk configuration

In this subsection, the number of actuator disks is fixed at three and only the radial thrust distribution is varied. The *strong inner weighting* configuration corresponds to a thrust split of 15%–15%–70% over

the outer, middle and inner disks, such that 70% of the thrust is produced by the smallest disk located largely within the boundary layer. The *equal loading* case distributes thrust uniformly over all three disks (33%–33%–33%). The *moderate inner weighting* configuration uses a thrust split of 25%–25%–50%. The resulting normalised power differences are summarised in Table 5.3.

Table 5.3: Normalised downstream–freestream power-flux differences for the three-disk configuration with varying thrust weighting towards the inner part of the actuator disk.

Configuration	$\widehat{\Delta P}_{\mathrm{down-free}}$ [-]
Inner weighting (15% / 15% / 70%)	0.021
Moderate inner weighting (25% / 25% / 50%)	0.027
Equal loading (33% / 33% / 33%)	0.032

The normalised downstream–freestream power-flux difference decreases as a larger fraction of the thrust is produced within the boundary layer. For the equal-loading configuration, the slipstream contains approximately 3.2% more kinetic power than the undisturbed tunnel flow. This excess decreases to 2.7% for the moderate inner weighting and to 2.1% when most of the thrust is generated by the inner disk.

These results indicate that, for a fixed number of actuator disks, shifting thrust production towards the boundary layer reduces the fraction of added power that is convected into the outer flow. As a result, a larger portion of the actuator power is used to re-energise the boundary-layer flow rather than increasing the kinetic energy of the surrounding freestream.

5.5.3. Combined interpretation of power-flux results

The power-flux analysis is used to compare actuator-disk layouts and radial thrust distributions in terms of the power required by the actuator system and the amount of surplus kinetic energy convected into the slipstream.

Increasing the number of actuator disks while keeping the operating condition and thrust per unit area fixed leads to a reduction in the normalised upstream–downstream power difference $\widehat{\Delta P}_{\mathrm{down-up}}$. For effectively the same thrust, multi-disk configurations therefore require a smaller relative power input between the upstream and downstream planes.

For a fixed number of disks, the three-disk weighting study shows that the normalised downstream–freestream power difference $\widehat{\Delta P}_{\mathrm{down-free}}$ decreases as thrust is shifted towards the boundary layer. Concentrating thrust production on the inner disk reduces the amount of excess kinetic energy present in the slipstream relative to a clean tunnel, while the upstream–downstream power addition remains nearly unchanged.

These results indicate that combining a multi-disk actuator layout with thrust weighting towards the boundary layer reduces both the relative power input required for a given thrust and the fraction of that power that is convected into the outer flow as surplus slipstream kinetic energy.

6

Inverse Blade Design

This chapter presents the inverse blade-design framework used to translate a prescribed actuator-disk loading into a propeller geometry. The method takes the radial pressure-jump distribution $\Delta p(r)$ obtained from the coupled BLI actuator-disk model and converts it into a target annular thrust distribution, which is then matched using a BEM formulation. The resulting chord and twist distributions are used to construct a three-dimensional propeller geometry and to provide consistent blade-level interpretations of the disk-level loading strategies analysed in this thesis.

6.1. Overview and Objective

The inverse blade-design model connects a prescribed actuator-disk loading to a three-dimensional propeller geometry and associated spanwise loads. The process is organised in three blocks (Figure 6.1):

1. preprocessing of the actuator-disk pressure jump and its translation into a target annular thrust distribution;
2. spanwise inverse design using a drag-aware BEM formulation;
3. three-dimensional blade construction and basic performance evaluation.

The inputs are chosen to be consistent with the actuator-disk boundary-layer-ingestion (BLI) analysis. They include the operating condition (density, freestream speed, rotational speed and number of blades), an axial inflow profile $U_{\mathrm{in}}(r)$ at the disk plane, and two-dimensional airfoil polars generated with XFOIL. The multiple disk actuator-disk model supplies a table of radii and pressure jumps $[r_i, \Delta p_i]$, which is interpolated and filtered to obtain a smooth radial pressure jump distribution $\Delta p(r)$. From this distribution the annular thrust $\mathrm{d}T/\mathrm{d}r = 2\pi r \Delta p(r)$ is computed. This is the target spanwise thrust that the blade must reproduce.

In the spanwise inverse design, the blade is discretised into radial stations. At each radius r, the local inflow $U_{\mathrm{in}}(r)$, the tangential speed Ωr and the assigned airfoil polar define the local aerodynamic environment. For each station, a BEM-based inner loop iterates on induction factors and chord such that the net aerodynamic thrust per unit radius matches the target $\mathrm{d}T/\mathrm{d}r$ implied by $\Delta p(r)$. This yields distributions of chord, twist, induction factors and load along the span.

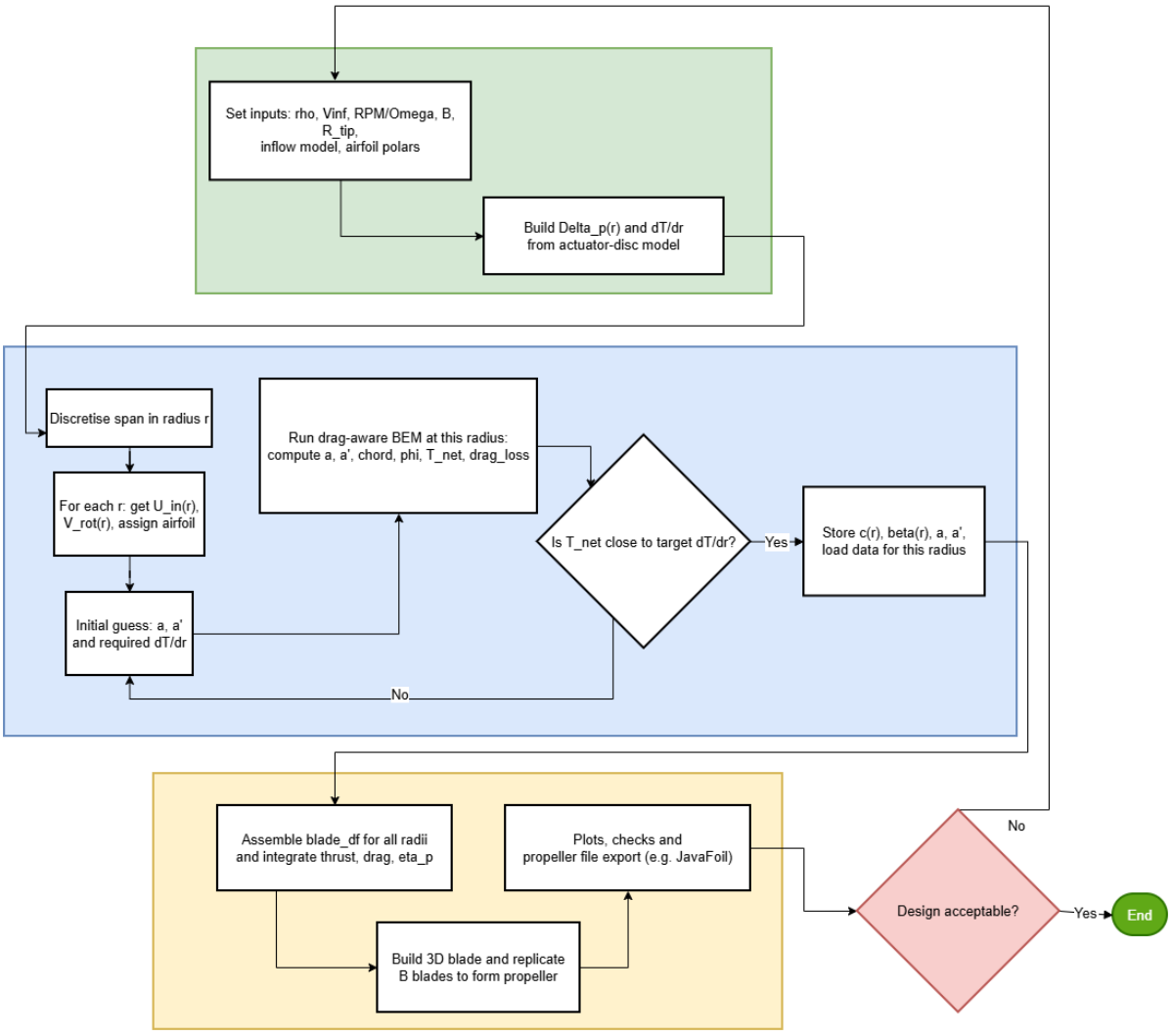

Figure 6.1: Flow of the inverse blade-design methodology.

In the final block, the spanwise geometry is converted into a 3D blade by scaling and rotating airfoil sections at each radius, and then replicating the blade B times by azimuthal rotation to form the propeller. The spanwise thrust and drag distributions are integrated to obtain total thrust, propeller drag and a simple propulsive efficiency. Diagnostic plots of $\Delta p(r)$, thrust split, chord and twist distributions, spanwise loads and the 3D geometry are generated. The workflow supports iterative changes to $\Delta p(r)$, inflow and airfoil selection to study how actuator-disk loadings and BLI conditions translate into blade shapes and performance.

6.2. Inputs from the actuator-disk BLI model

The inverse blade-design model is coupled to the BLI actuator-disk analysis through the radial pressure jump distribution across the disk. All other inputs are specified locally in the blade-design framework.

From the actuator-disk model, a table of radii and pressure jumps $[r_i, \Delta p_i]$ is obtained. Each entry represents the mean pressure rise produced by one of the disks in the multiple-disk representation up to its outer radius. In the inverse design this table is interpreted as the desired radial pressure jump distribution at the design condition.

Inside the blade-design code, $[r_i, \Delta p_i]$ is interpolated onto a fine radial grid from a root radius to the tip radius R_{tip}. Linear interpolation yields a continuous curve $\Delta p(r)$. A mild Gaussian-type filter in radius removes sharp changes between adjacent grid points, while preserving the overall shape of the actuator-disk design (e.g. an approximately elliptical profile and the prescribed split between inner and outer loading).

The corresponding annular thrust distribution is

$$\frac{\mathrm{d}T}{\mathrm{d}r}(r) = 2\pi r\,\Delta p(r),$$

which is the net axial force per unit radius that all blades together must generate at radius r. This distribution is taken as the target for the inverse BEM solution.

All remaining inputs are defined within the blade-design framework: density ρ, design freestream velocity V_∞, rotational speed Ω (or RPM), number of blades B, root and tip radii, target Reynolds number for the airfoil polars and the choice of airfoil families along the span. The axial inflow profile $U_{\text{in}}(r)$ at the disk plane is also specified analytically: reduced axial velocity is prescribed in an inner "boundary-layer" region and a constant value equal to V_∞ outside. This profile mimics a BLI inflow but is not taken directly from the coupled boundary-layer and wake simulation.

In summary, the inverse blade design receives $\Delta p(r)$ from the BLI actuator-disk model and uses it to fix the radial thrust loading at the design condition. Other parameters (rotation, inflow idealisation and airfoil choice) are set independently to explore different design combinations.

6.3. Spanwise inverse design

The spanwise inverse design maps the prescribed $\Delta p(r)$ and $U_{\text{in}}(r)$ to chord and twist distributions along the blade using a drag-aware blade-element–momentum (BEM) formulation.

The blade span from root to tip is divided into radial stations. At each station the inflow $U_{\text{in}}(r)$, rotational speed Ωr and airfoil type are known. The target net thrust per unit radius is

$$\left(\frac{\mathrm{d}T}{\mathrm{d}r}\right)_{\text{target}} = 2\pi r\,\Delta p(r),$$

interpreted as the sum of axial forces from all blades in a thin annulus at radius r.

For a given station, the blade element sees local velocities

$$V_{\text{ax}} = U_{\text{in}}(r)\,(1-a)\,, \qquad V_{\tan} = \Omega r\,(1+a')\,,$$

with axial and tangential induction factors a and a'. The relative speed and inflow angle are

$$V_{\text{rel}} = \sqrt{V_{\text{ax}}^2 + V_{\tan}^2}, \qquad \phi = \arctan\!\left(\frac{V_{\text{ax}}}{V_{\tan}}\right).$$

For the chosen airfoil, the lift and drag coefficients C_L and C_D at the design angle of attack are taken from the polars. The normal and tangential coefficients relative to the disk plane are

$$C_n = C_L\cos\phi - C_D\sin\phi, \qquad C_t = C_L\sin\phi + C_D\cos\phi.$$

The annular thrust from all blades is

$$\left(\frac{\mathrm{d}T}{\mathrm{d}r}\right)_{\text{aero}} = B\,\frac{1}{2}\rho V_{\text{rel}}^2\,c(r)\,C_n,$$

with unknown chord $c(r)$.

The inverse problem at each radius is to find a, a' and $c(r)$ such that $(\mathrm{d}T/\mathrm{d}r)_{\text{aero}} = (\mathrm{d}T/\mathrm{d}r)_{\text{target}}$. This is solved by a two-level iteration. For a given required thrust $(\mathrm{d}T/\mathrm{d}r)_{\text{req}}$, an inner loop solves the BEM equations for a, a' and $c(r)$; an outer loop adjusts $(\mathrm{d}T/\mathrm{d}r)_{\text{req}}$ until the resulting aerodynamic thrust matches the actuator-disk target.

In the inner loop, an initial guess for a and a' is used to compute V_{ax}, $V_{\tan}$, V_{rel} and ϕ, and hence C_n and C_t. The chord required to produce the prescribed $(\mathrm{d}T/\mathrm{d}r)_{\text{req}}$ is

$$c(r) = \frac{(\mathrm{d}T/\mathrm{d}r)_{\text{req}}}{B\,\frac{1}{2}\rho V_{\mathrm{rel}}^2 C_n}.$$

With this chord, the torque and induced velocities are evaluated and a and a' are updated from the momentum relations for axial and tangential induction (including a high-thrust correction and relaxation for convergence). The process is repeated until changes in a and a' between iterations are small.

After inner-loop convergence, the aerodynamic thrust $(\mathrm{d}T/\mathrm{d}r)_{\text{aero}}$ is compared to $(\mathrm{d}T/\mathrm{d}r)_{\text{target}}$. If the mismatch exceeds a tolerance, $(\mathrm{d}T/\mathrm{d}r)_{\text{req}}$ is adjusted and the inner loop is repeated. When the blade element thrust agrees with the target, the chord, inflow angle, induction factors and local thrust and drag are stored. The local blade pitch angle is $\beta(r) = \phi(r) + \alpha_{\text{design}}$.

Repeating this procedure over all radial stations yields spanwise distributions of chord $c(r)$, twist $\beta(r)$, induction factors $a(r)$, $a'(r)$ and loads. These form the input for the 3D geometry reconstruction and performance evaluation.

6.4. Three-dimensional blade geometry and performance

The 3D blade is constructed by placing airfoil sections along the span based on the spanwise inverse-design results. For each radial station, the selected airfoil coordinates are scaled to the local chord $c(r)$, rotated by the local twist $\beta(r)$ and translated to the radius r. Lofting these sections gives a single blade. Replicating this blade B times by rotation about the axis produces the complete propeller. The code exports this geometry and a propeller definition file for use in external tools such as JavaFoil or JavaProp.

At each radial station the model evaluates a net thrust per unit span $T_{\text{net}}(r)$ and a corresponding propeller drag contribution $D_{\text{prop}}(r)$. The thrust includes drag effects via the normal force coefficient C_n; the drag represents the axial component of profile drag. Integrating these distributions gives the total thrust and total propeller drag:

$$T_{\text{tot}} = \int_{r_{\text{root}}}^{R_{\text{tip}}} T_{\text{net}}(r)\,\mathrm{d}r, \qquad D_{\text{prop}} = \int_{r_{\text{root}}}^{R_{\text{tip}}} D_{\text{prop}}(r)\,\mathrm{d}r.$$

A simple propulsive efficiency is defined as

$$\eta_p = \frac{T_{\text{tot}}}{T_{\text{tot}} + D_{\text{prop}}},$$

which indicates what fraction of the axial force is available as useful thrust versus being lost as self-induced drag.

The model also generates diagnostic plots: $\Delta p(r)$ and the thrust split between inner and outer regions, chord and twist distributions, spanwise thrust and drag, and 3D views of the blade and propeller. These outputs link disk-level choices such as the shape of $\Delta p(r)$ to blade-level quantities and basic performance indicators.

6.5. Limitations of the framework

The inverse blade-design framework is intended as a bridge between the actuator-disk BLI analysis and practical propeller geometries. It relies on several simplifying assumptions:

- **Aerodynamic model.** The method uses steady blade-element–momentum theory at a single operating point. It includes profile drag and a high-thrust correction, but does not model unsteady effects, detailed 3D flow or tip-vortex dynamics. The inflow is axisymmetric and each radial station is solved independently.
- **Inflow profile.** The inflow at the disk is represented by an analytical boundary-layer-like profile with a sharp transition between ingested and outer regions. It reflects the presence of a low-momentum inner region but does not reproduce the detailed velocity and turbulence structure of the full BLI inflow.
- **Airfoil data.** Airfoil characteristics are taken from 2D viscous polars at a single Reynolds number and fixed design angle of attack. Variations in Reynolds number along the span, off-design angles and 3D corrections are not included, and the spanwise airfoil distribution is prescribed rather than optimised.
- **Operating-point coverage.** The inverse design is carried out for one design condition. The blade reproduces the desired loading at that condition; behaviour at other advance ratios or flight points is not assessed.
- **One-way coupling.** The coupling between actuator-disk model and inverse design is one-way. The actuator-disk solution defines $\Delta p(r)$ and the inflow idealisation; the blade is then designed to match this radial thrust. The resulting blade is not fed back into the actuator-disk and boundary-layer model, so consistency is enforced at the level of annular thrust only, not via a fully coupled flow solution.

Within these limits, the framework provides a systematic way to translate actuator-disk pressure jump distributions, obtained for different BLI scenarios, into propeller geometries and spanwise loading patterns. This enables the actuator-disk and wake-analysis trends to be interpreted in terms of concrete blade shapes and prepares the ground for future extensions with higher-fidelity aerodynamics and structural or manufacturability constraints.

7

Blade Design Results

This chapter presents the results from the inverse blade design methodology that has been described in chapter 6. First, the different prescribed pressure jumps are given in section 7.1 and following that all the results are shown.

7.1. Prescribed pressure-jump distributions

The inverse blade designs in this chapter are generated from prescribed radial pressure-jump distributions, $\Delta p(r)$, which define the actuator-disk loading. The cases are compared at the same actuator-disk radius and imposed thrust level, so that differences in the resulting blade geometry can be attributed to the shape of $\Delta p(r)$. In all cases, the total thrust is prescribed by the coupled actuator-disk model and kept constant. Each $\Delta p(r)$ profile is scaled to satisfy the same disk-integrated thrust, so only the radial redistribution of loading differs between cases.

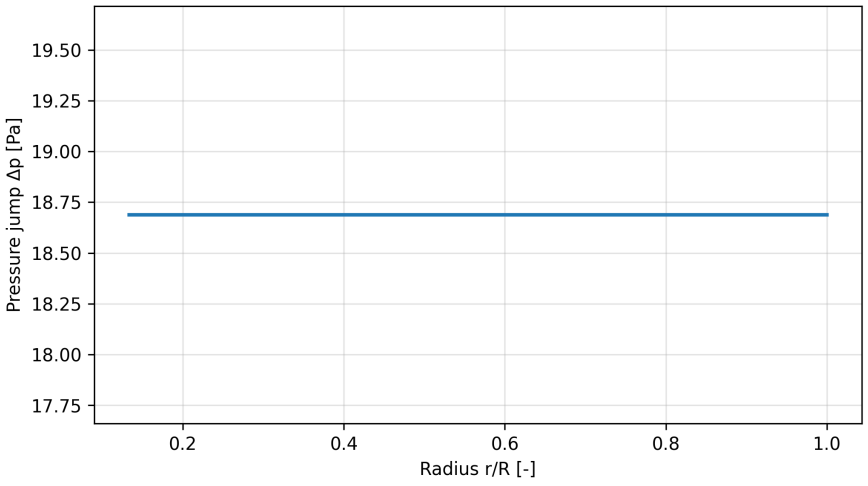

Figure 7.1: Prescribed constant pressure-jump distribution.

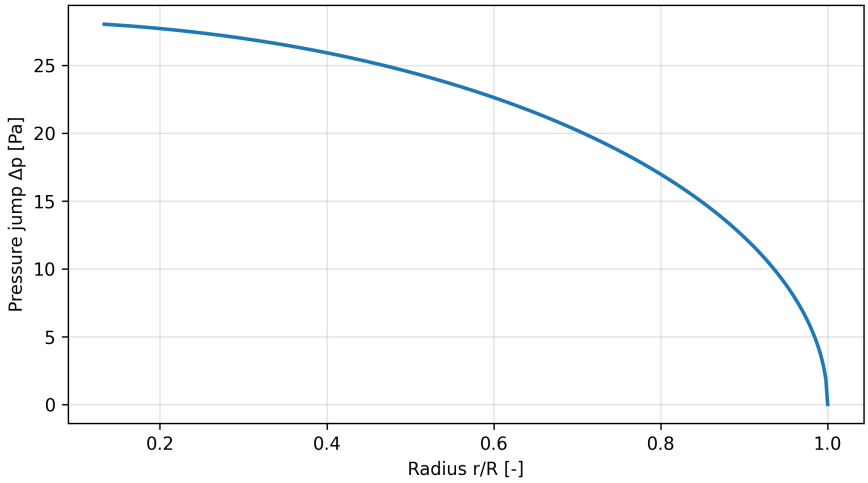

Figure 7.2: Prescribed Elliptical Pressure Jump.

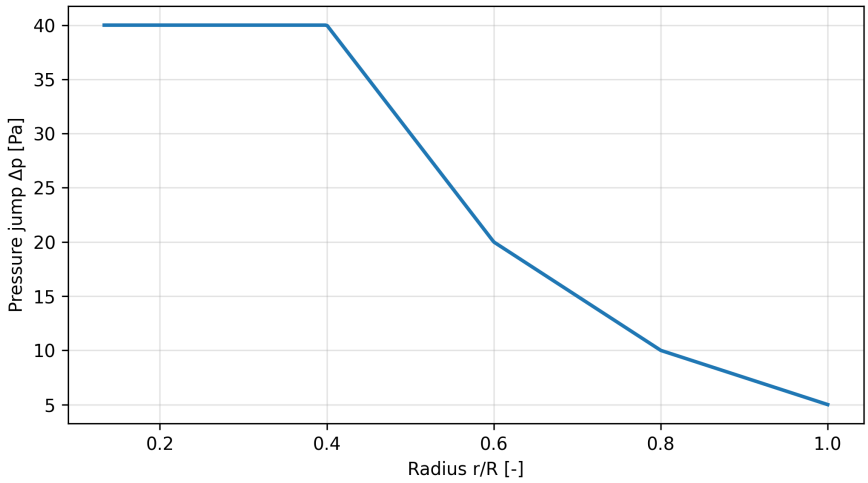

Figure 7.3: Prescribed four stepped pressure-jump distribution. The loading is biased towards the inboard radii corresponding to the boundary-layer region, so that a larger fraction of the total thrust is generated where the inflow deficit is strongest.

7.2. Constant Pressure Jump

This section presents blades designed for a radially uniform pressure jump and compares the effect of the inflow profile. By keeping the pressure jump fixed and only changing from a uniform to a boundary layer inflow, the sensitivity of the blade geometry to the ingested velocity deficit can be isolated.

Constant pressure jump with uniform inflow

The constant pressure jump design under uniform inflow produces a smoothly decreasing chord, with the highest chord concentrated near the root and a gradual taper towards the tip. The twist distribution is fixed for all designs and decreases almost linearly from about 90° at the root to 40° at the tip, so the local loading variation is carried primarily by the chord. This behaviour is visible in Figure 7.4, where the chord and twist distribution in Figure 7.4a translates into a relatively slender planform with most of the area located inboard, as shown in Figure 7.4b.

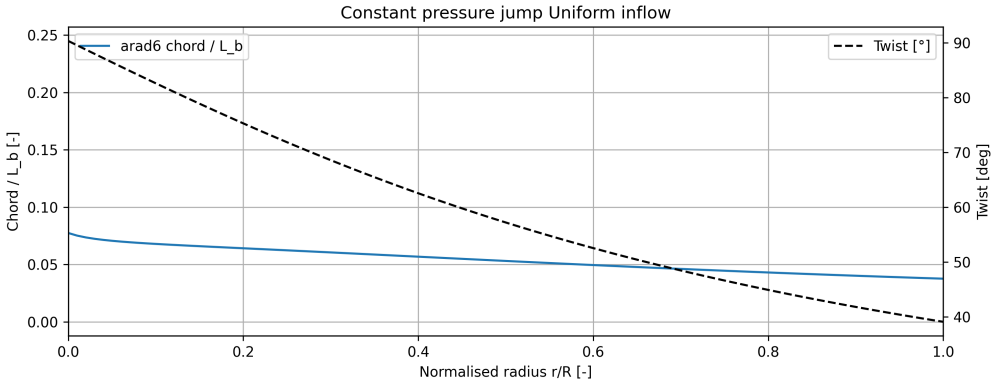

(a) Chord and twist distribution.

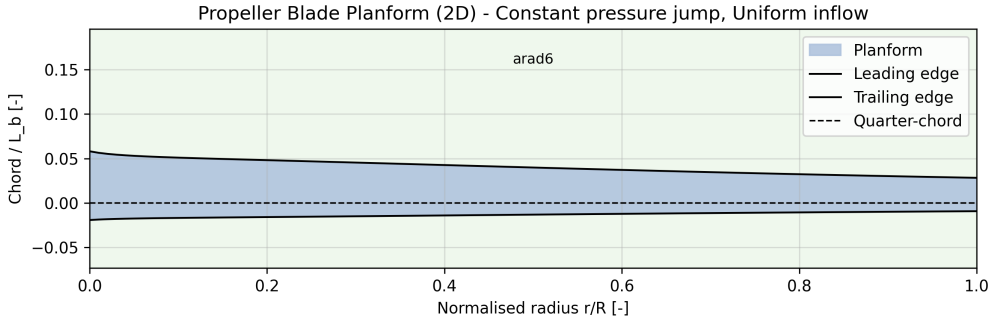

(b) Two dimensional planform

Figure 7.4: Constant pressure jump blade design under uniform inflow: (a) chord and twist distribution, (b) corresponding two-dimensional planform.

Constant pressure jump with boundary layer inflow

When the same constant pressure jump is imposed in boundary layer inflow, the inner blade sections require more area to compensate for the reduced axial velocity. This leads to a noticeably higher inboard chord compared to the uniform inflow case, while the outer part of the blade converges to a similar chord level and retains the same monotonic twist schedule. Figure 7.5 illustrates this inboard thickening in the chord and twist distribution in Figure 7.5a, which manifests as a fuller root region in the planform in Figure 7.5b, concentrating blade area where the ingested flow has the lowest momentum.

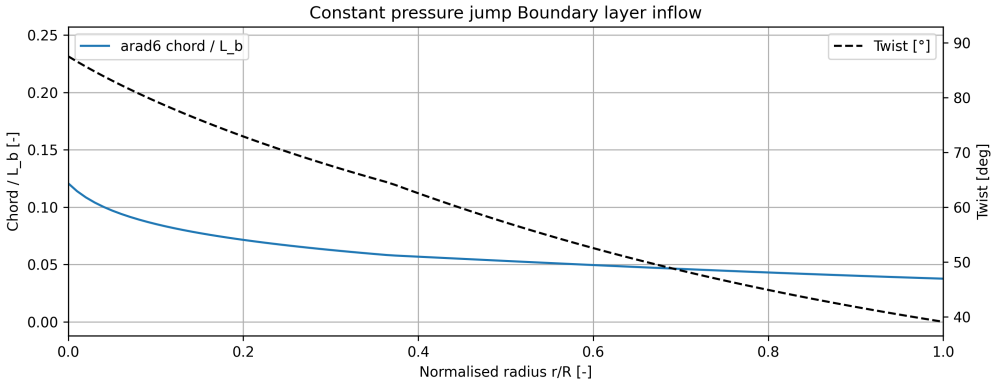

(a) Chord and twist distribution.

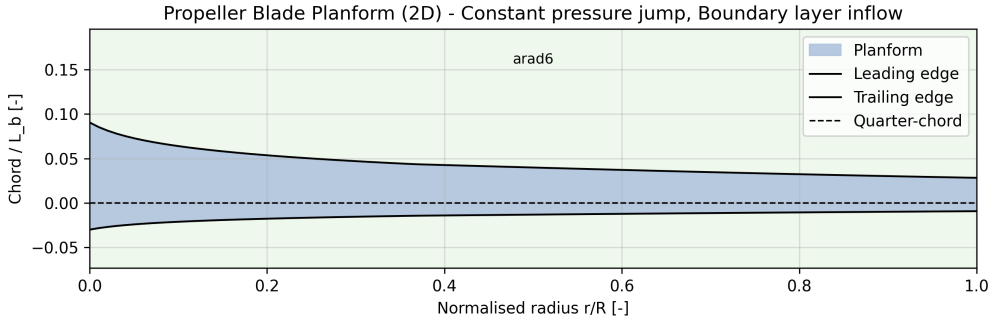

(b) Two dimensional planform.

Figure 7.5: Constant pressure jump blade design under boundary layer inflow: (a) chord and twist distribution, (b) corresponding two dimensional planform.

7.3. Pressure jump produced by four actuator disks

Here, the pressure jump is distributed in four discrete radial bands to emulate a more tailored loading while remaining compatible with the multi actuator disk model. Comparing uniform and boundary layer inflow again highlights how the same stepped loading leads to different geometric adaptations depending on the local inflow conditions.

Four-step pressure jump with uniform inflow

For the four-step pressure jump design in uniform inflow, the chord distribution shows clear changes in slope at the radii where the prescribed loading changes. Chord levels are increased in the more heavily loaded radial bands but still taper smoothly towards the tip, while the twist distribution remains identical to the constant pressure jump case. These stepwise changes are evident in Figure 7.6: the chord and twist plot in Figure 7.6a directly maps onto subtle variations in local blade width in the planform shown in Figure 7.6b.

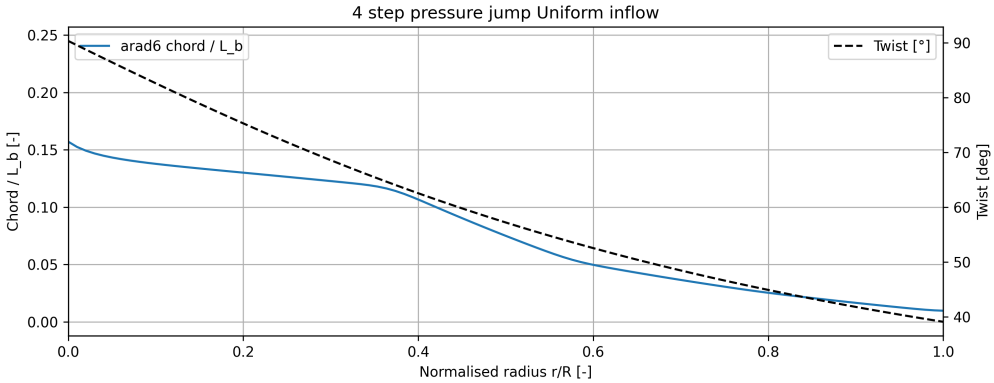

(a) Chord and twist distribution.

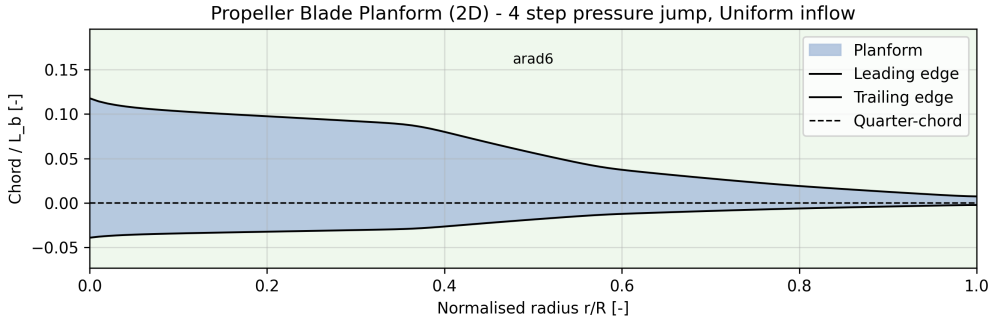

(b) Two dimensional planform.

Figure 7.6: Four step pressure jump blade design under uniform inflow: (a) chord and twist distribution, (b) corresponding two dimensional planform.

Four-step pressure jump with boundary layer inflow

In boundary layer inflow, the four step pressure jump blade combines an inboard chord build up with increased chord where the local pressure jump is higher. Blade area is therefore concentrated both near the root and in the higher loaded radial segments, while the underlying twist schedule is unchanged. As shown in Figure 7.7, the chord and twist distribution in Figure 7.7a results in a visibly broader inner blade and pronounced chord variations in the planform of Figure 7.7b.

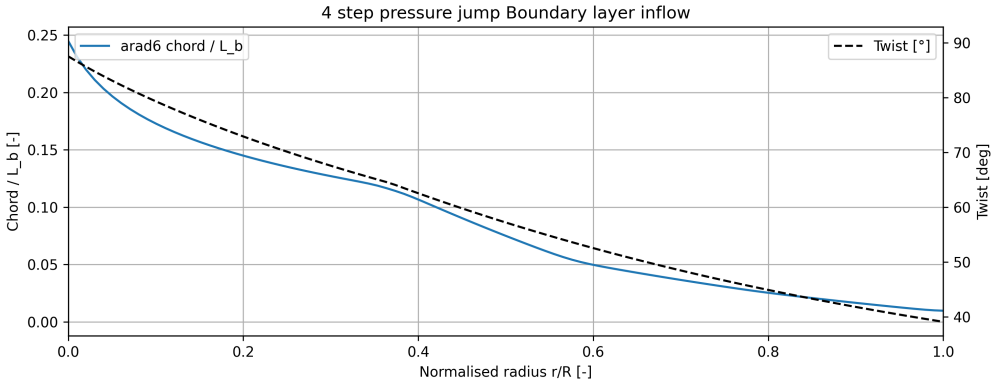

(a) Chord and twist distribution.

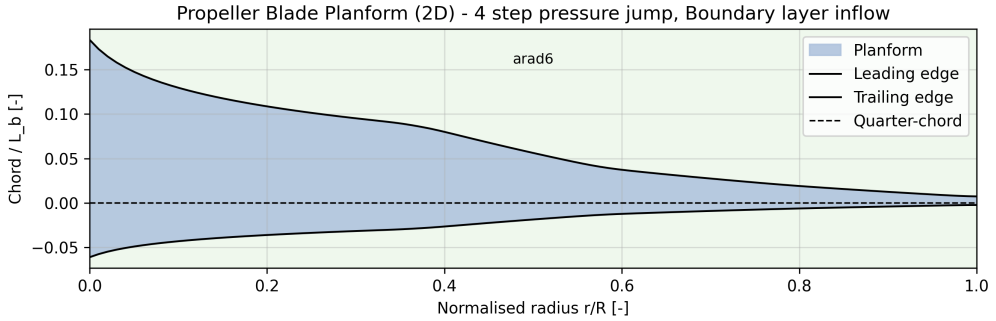

(b) Two dimensional planform.

Figure 7.7: Four step pressure jump blade design under boundary layer inflow: (a) chord and twist distribution, (b) corresponding two dimensional planform.

7.4. Elliptical Distribution

The final set of designs targets an approximately elliptical radial loading, which is closer to the theoretical optimum for minimizing induced losses. Within this family, the impact of ingesting a boundary layer is assessed by comparing the geometry obtained for uniform versus boundary layer inflow while keeping the underlying pressure jump shape consistent.

Elliptical distribution with uniform inflow

For the elliptical pressure jump design in uniform inflow, the chord distribution is more strongly weighted towards mid span compared to the constant pressure jump blade. The chord tapers smoothly from root to tip while the twist again decreases almost linearly, yielding a radial loading that more closely approaches the ideal elliptical distribution. Figure 7.8 shows how this manifests as a relatively broad mid span region in the chord and twist distribution in Figure 7.8a and a more pronounced taper towards the tip in the planform in Figure 7.8b.

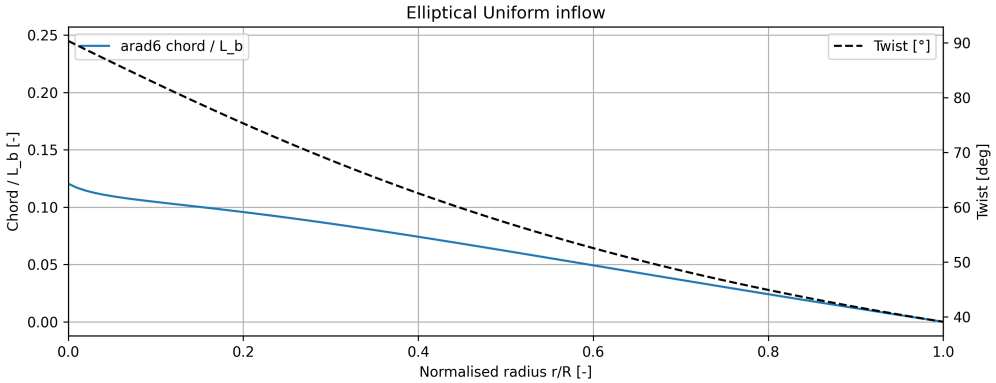

(a) Chord and twist distribution.

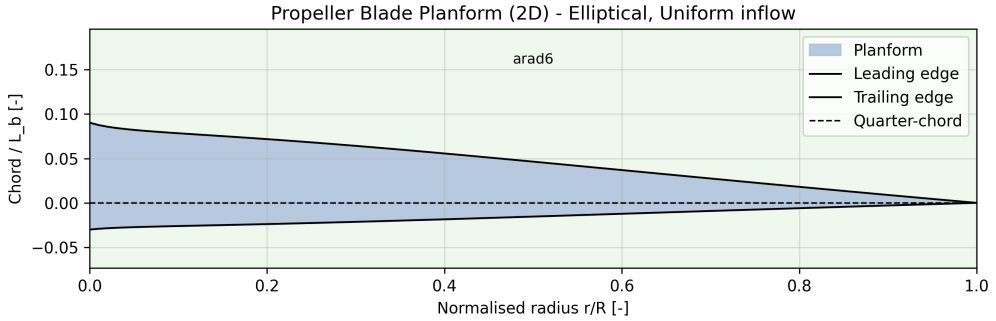

(b) Two dimensional planform.

Figure 7.8: Elliptical pressure jump blade design under uniform inflow: (a) chord and twist distribution, (b) corresponding two dimensional planform.

Elliptical distribution with boundary layer inflow

With boundary layer inflow, the elliptical pressure jump design develops a significantly larger chord in the inboard region, where both the prescribed loading and the inflow deficit are highest. The blade area is therefore concentrated where it can most effectively recover the low momentum boundary layer flow, while the twist still decreases monotonically towards the tip. This effect is visible in Figure 7.9: the chord and twist distribution in Figure 7.9a shows a strong inboard thickening, which translates into a noticeably fuller root region in the planform in Figure 7.9b, clearly distinguishing it from the uniform inflow elliptical blade.

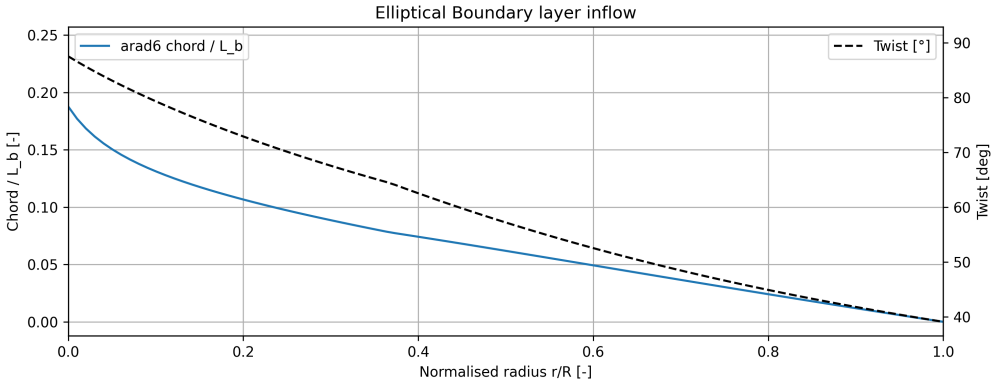

(a) Chord and twist distribution.

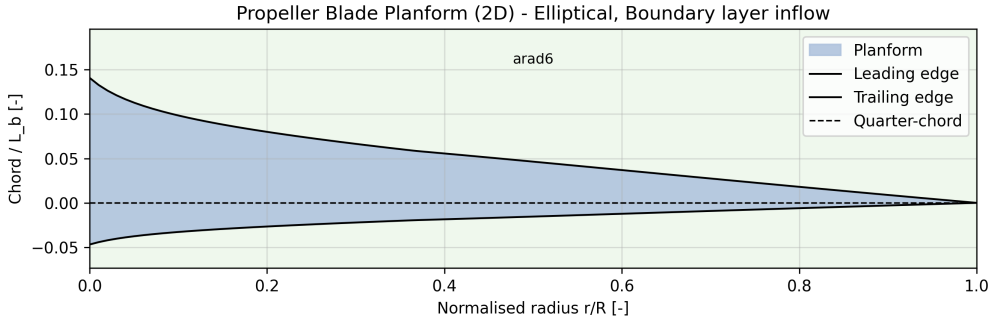

(b) Two dimensional planform.

Figure 7.9: Elliptical pressure jump blade design under boundary layer inflow: (a) chord and twist distribution, (b) corresponding two dimensional planform.

8

Validation

To validate the inverse blade design methodology, the resulting blade geometry is compared to the boundary-layer-ingesting propeller designed by Barara et al. [5] for the APPU project. As the two designs correspond to different missions and design objectives, the comparison is qualitative and focuses on geometric trends rather than performance metrics.

Figure 8.1 shows an overlay of the two blade planforms in a common coordinate system. Both blades exhibit an increase in chord within the boundary-layer region and a gradual reduction in chord towards the tip. In addition, the radial extent of the blades is similar, indicating comparable overall blade lengths despite the differing design requirements.

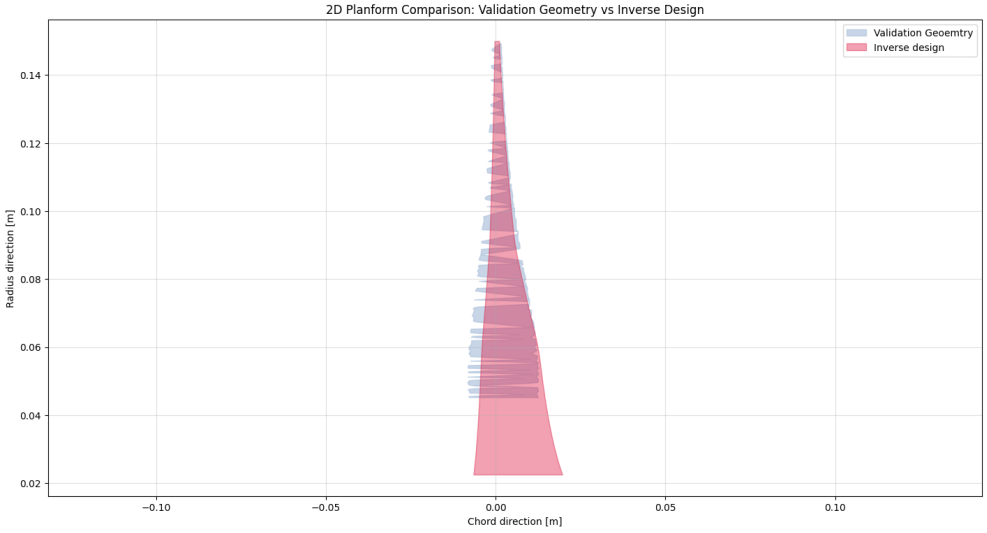

Figure 8.1: Overlay of the present blade planform and a reference blade designed for boundary-layer ingestion [5] in a common coordinate system.

The most pronounced difference is observed near the hub. The blade designed by Barara et al. features a larger hub radius and an approximately constant chord in the inboard region, which results from structural and manufacturing constraints imposed in that design. In contrast, the blade generated using

the present inverse design method is based solely on aerodynamic considerations. As no structural constraints are imposed, the root chord is allowed to decrease further.

A quantitative comparison of the chord distributions is shown in Figure 8.2. The blade designed in this thesis exhibits consistently smaller chord lengths than the reference blade. This difference may be attributed to the iterative coupling between the actuator-disk model and the upstream flow field used in the present approach, which explicitly accounts for the modification of the inflow caused by the propulsor itself.

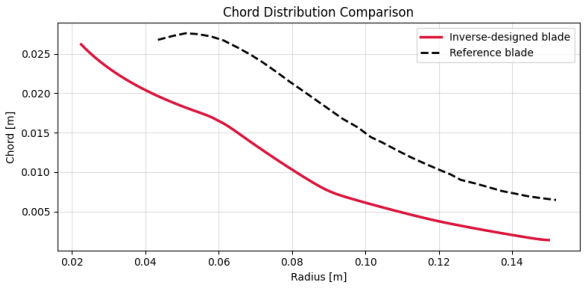

Figure 8.2: Comparison of the chord distribution of the present blade and the reference blade [5].

Figure 8.3 shows the comparison of the thickness distribution along the span of the blade. This does show quite a bit of difference compares to the reference design, but it should be kept in mind that the mission that both of these designed for are completely different.

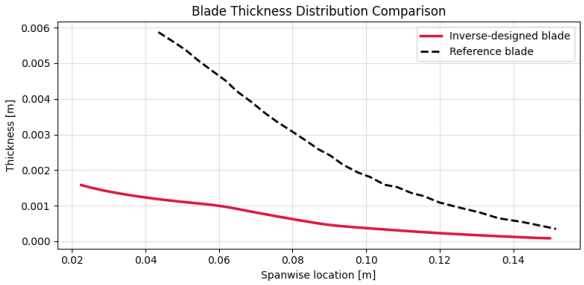

Figure 8.3: Comparison of the thickness distribution of the present blade and the reference blade [5].

Overall, the agreement in chord build-up within the boundary layer and the similarity in overall blade length indicate that the present inverse design method produces a realistic blade geometry for boundary-layer-ingesting propellers.

9

Conclusion

This thesis investigated the influence of radial pressure-jump distribution on the aerodynamic performance of a boundary layer ingestion propulsor. A coupled actuator-disk and boundary-layer framework was used to analyse slipstream mixing losses, power-flux behaviour, and the implications for propeller blade design. The main conclusions are summarised below.

- **Approximation of elliptical loading.** Increasing the number of actuator disks results in a stepped pressure-jump distribution that more closely approximates an elliptical distribution. This provides a practical way to represent non-uniform radial loading within the actuator-disk framework while retaining control over the thrust distribution.
- **Reduction of slipstream mixing losses.** The mixing-loss analysis shows that slipstream mixing losses decrease as the pressure-jump distribution becomes more elliptical. Uniform pressure-jump distributions generate strong radial velocity gradients in the slipstream, which persist downstream and lead to increased irreversible losses. As the loading is redistributed toward an elliptical shape, these gradients are reduced.
- **Downstream–upstream power-flux behaviour.** The downstream-minus-upstream power flux decreases as the number of actuator disks is increased. This indicates that a larger fraction of the propulsor work is extracted from the low-momentum flow inside the boundary layer rather than from the freestream.
- **Downstream–freestream power-flux behaviour.** The downstream-minus-freestream power flux decreases as the thrust distribution is shifted toward the centre of the disk. This shows that the downstream flow approaches the undisturbed freestream condition more closely, reducing excess kinetic energy in the slipstream and associated losses.
- **Preferred actuator-disk configuration.** Based on the combined mixing-loss and power-flux results, a four-disk actuator model with thrust concentrated in the boundary layer provides the most favourable configuration among those studied.
- **Implications for blade design.** Using the selected actuator-disk configuration, a propeller blade was designed. The resulting blade geometry reflects the non-uniform inflow and loading associated with boundary layer ingestion and shows strong qualitative similarity to an existing blade designed for this purpose, while differing clearly from blades intended for undisturbed, uniform

inflow.

In conclusion, this work demonstrates that shaping the radial pressure-jump distribution is a key mechanism for reducing aerodynamic losses in boundary layer ingestion propulsors. The coupled analysis and inverse blade design approach developed in this thesis provides a consistent and physically grounded basis for future design and optimisation studies, which are discussed in the following chapter.

10

Recommendations and Future Work

The results presented in this thesis demonstrate that redistributing the actuator-disk loading can influence slipstream structure and the associated losses in a boundary-layer-ingesting configuration. While the developed coupled framework enables rapid comparison of loading strategies and inverse blade design, several extensions are recommended to improve physical fidelity, increase confidence in the predicted trends, and broaden applicability to realistic propulsor designs.

- **Validate the loss trends.** Compare the power-flux / mixing-loss metrics against higher-fidelity simulations (RANS/URANS) and/or available wind-tunnel data to confirm that the ranking of loading distributions remains consistent.
- **Increase actuator-disk fidelity.** Extend the actuator-disk model to include swirl/torque and (if required) tip-loss and profile-loss corrections, so that shaft power and wake structure are represented more realistically.
- **Improve wake recovery modelling.** Replace purely numerical smoothing with a simple physics-based wake growth/mixing model (e.g. a diffusion-inspired wake spreading formulation) to reduce sensitivity to discretisation and control-point placement.
- **Optimise $\Delta p(r)$ continuously.** Formulate a constrained optimisation problem where $\Delta p(r)$ is parameterised (e.g. splines) and chosen to minimise a loss objective at fixed thrust, with bounds on peak loading and smoothness/manufacturability constraints.
- **Constrain inverse blade design.** Enforce airfoil polar limits (stall margin), minimum thickness/spar volume, and chord/twist smoothness so the designed blades remain feasible.

References

[1] A. F. Abad. *Experimental Validation of an Aerodynamic Sectional Modeling Approach in Fixed-Wing Unmanned Aerial Vehicles*. Scientific Figure on ResearchGate. Available from: https://www.researchgate.net/figure/Theory-of-actuator-disk_fig6_329383364 [accessed 20 Mar 2025]. 2025.

[2] Nando van Arnhem. "Design and Analysis of an Installed Pusher Propeller with Boundary Layer Inflow". MA thesis. Delft University of Technology, 2015. URL: http://resolver.tudelft.nl/uuid:367bcf1f-2f37-421c-a4d0-b8086f120799.

[3] Nando van Arnhem et al. "Engineering Method to Estimate the Blade Loading of Propellers in Nonuniform Flow". In: *AIAA Journal* 58.12 (2020), pp. 5332–5346. DOI: 10.2514/1.J059666.

[4] Aurélien Arntz et al. "Exergy-based Aircraft Aeropropulsive Performance Assessment: CFD Application to Boundary Layer Ingestion". In: *32nd AIAA Applied Aerodynamics Conference*. 2014. DOI: 10.2514/6.2014-2573. eprint: https://arc.aiaa.org/doi/pdf/10.2514/6.2014-2573. URL: https://arc.aiaa.org/doi/abs/10.2514/6.2014-2573.

[5] Daamanjyot Barara, Martijn van Sluis, and Tomas Sinnige. "Impact of Installation Effects on Optimal Propeller Design: Application to a Boundary-Layer-Ingesting Propeller". In: *AIAA Aviation Forum and ASCEND 2024*. Las Vegas, NV, USA: American Institute of Aeronautics and Astronautics, July 2024. DOI: 10.2514/6.2024-3522.

[6] H. Blasius. *Boundary Layers in Fluids with Little Friction (Translation of "Grenzschichten in Flüssigkeiten mit kleiner Reibung", 1908)*. Tech. rep. Technical Memorandum 1256. National Advisory Committee for Aeronautics (NACA), 1950.

[7] D. G. M. Davis and R. M. Bass. "A Review of Some Recent U.K. Propeller Developments". In: *AIAA/SAE/ASME/ASEE 21st Joint Propulsion Conference*. Monterey, CA, USA, 1985. DOI: 10.2514/6.1985-1261.

[8] M. Drela. "Development of the D8 Transport Configuration". In: *29th AIAA Applied Aerodynamics Conference*. June 2011, p. 3970. DOI: 10.2514/6.2011-3970.

[9] Mark Drela. "Power Balance in Aerodynamic Flows". In: *AIAA Journal* 47.7 (2009), pp. 1761–1771. DOI: 10.2514/1.42409.

[10] H. Glauert. *Airplane Propellers*. Ed. by W. F. Durand. Springer, 1935.

[11] E. M. Greitzer et al. *N+3 Aircraft Concept Designs and Trade Studies, Final Report Volume 1*. Tech. rep. NASA/CR—2010-216794/VOL1. NASA Glenn Research Center, Dec. 2010. URL: https://ntrs.nasa.gov/citations/20100042401.

[12] David K. Hall et al. "Boundary Layer Ingestion Propulsion Benefit for Transport Aircraft". In: *Journal of Propulsion and Power* 33.5 (2017), pp. 1118–1129. DOI: 10.2514/1.B36321.

[13] G. A. M. van Kuik and L. E. M. Lignarolo. "Potential Flow Solutions for Energy Extracting Actuator Disc Flows". In: *Wind Energy* 19.8 (2015), pp. 1391–1406. DOI: 10.1002/we.1902.

[14] G. A. M. Van Kuik. *The Fluid Dynamic Basis for Actuator Disc and Rotor Theories: Revised Second Edition*. IOS Press, 2022.

[15] Tomáš Kukučka. “Potential flow modelling of boundary layer ingesting configurations”. Graduation date: 22-06-2023. Master Thesis. Delft University of Technology, June 2023. URL: https://repository.tudelft.nl/record/uuid:5a4d3273-be89-4024-9ff6-7b63af71e5e8.

[16] J. Gordon Leishman. *Principles of Helicopter Aerodynamics*. 2nd ed. Cambridge University Press, 2006.

[17] Peijian Lv. “Theoretical and Experimental Investigation of Boundary Layer Ingestion for Aircraft Application”. Dissertation (TU Delft). Delft University of Technology, 2019. DOI: 10.4233/uuid:6d8bd168-e057-4ee9-854c-32c84015e4c4.

[18] H. C. McLemore. *Wind-Tunnel Tests of a 1/20-Scale Airship Model With Stern Propellers*. Technical Note TN-D-1026. National Aeronautics and Space Administration, Jan. 1962. URL: https://apps.dtic.mil/sti/citations/AD0270084.

[19] Angélique Plas. “Performance of a Boundary Layer Ingesting Propulsion System”. Master’s Thesis. Massachusetts Institute of Technology, 2006. URL: https://dspace.mit.edu/handle/1721.1/35568.

[20] Anton P. Plas et al. “Performance of a Boundary Layer Ingesting Propulsion System”. In: *45th AIAA Aerospace Sciences Meeting and Exhibit*. AIAA Paper 2007-450. 2007. DOI: 10.2514/6.2007-450.

[21] L. Prandtl. “Applications of modern hydrodynamics to aeronautics”. In: *NACA Technical Memorandum* 116 (1923).

[22] W. J. M. Rankine. “On the Mechanical Principles of the Action of Propellers”. In: *6th Session of the Institution of Naval Architects*. 1865, pp. 13–19.

[23] P. G. Saffman. *Vortex Dynamics*. Cambridge University Press, 1992.

[24] Hermann Schlichting and Klaus Gersten. *Boundary-Layer Theory*. 9th ed. Berlin, Heidelberg: Springer, 2017. DOI: 10.1007/978-3-662-52919-5.

[25] L. H. Smith Jr. “Wake ingestion propulsion benefit”. In: *Journal of Propulsion and Power* 9.1 (1993), pp. 74–82. DOI: 10.2514/3.11487.

[26] A. Uranga et al. “Boundary Layer Ingestion Benefit of the D8 Transport Aircraft”. In: *AIAA Journal* 55.11 (Nov. 2017), pp. 3693–3708. DOI: 10.2514/1.j055755.

[27] A. Uranga et al. “Preliminary Experimental Assessment of the Boundary Layer Ingestion Benefit for the D8 Aircraft”. In: *52nd Aerospace Sciences Meeting*. 2014, p. 0906. DOI: 10.2514/6.2014-0906.

[28] Alejandra Uranga et al. “Boundary Layer Ingestion Benefit of the D8 Transport Aircraft”. In: *AIAA Journal* 55.11 (2017). DOI: 10.2514/1.J055755.

[29] J. R. Welstead and J. L. Felder. “Conceptual Design of a Single-Aisle Turboelectric Commercial Transport with Fuselage Boundary Layer Ingestion”. In: *54th AIAA Aerospace Sciences Meeting*. 2016, p. 1027. DOI: 10.2514/6.2016-1027.

[30] L. Wiart et al. “Aeropropulsive Performance Analysis of the NOVA Configurations”. In: *30th Congress of the International Council of the Aeronautical Sciences*. Sept. 2016.